Advanced 3D Monte Carlo algorithms for bio-photonic and medical applications

Lewis McMillan

University of
St Andrews

This thesis is submitted in partial fulfilment for the degree of
PhD
at the
University of St Andrews

March 2019

Declaration

I, Lewis McMillan, hereby certify that this thesis, which is approximately ***** words in length, has been written by me, that it is the record of work carried out by me, or principally by myself in collaboration with others as acknowledged, and that it has not been submitted in any previous application for a higher degree.

I was admitted as a research student in September 2015 and as a candidate for the degree of PhD in September 2015; the higher study for which this is a record was carried out in the University of St Andrews between 2015 and 2019.

Date............................ Signature of candidate ....

I hereby certify that the candidate has fulfilled the conditions of the Resolution and Regulations appropriate for the degree of PhD in the University of St Andrews and that the candidate is qualified to submit this thesis in application for that degree.

Date .... Signature of supervisor ....

Date .... Signature of supervisor ....

Abstract

Lorem ipsum dolor sit amet, consectetuer adipiscing elit. Ut purus elit, vestibulum ut, placerat ac, adipiscing vitae, felis. Curabitur dictum gravida mauris. Nam arcu libero, nonummy eget, consectetuer id, vulputate a, magna. Donec vehicula augue eu neque. Pellentesque habitant morbi tristique senectus et netus et malesuada fames ac turpis egestas. Mauris ut leo. Cras viverra metus rhoncus sem. Nulla et lectus vestibulum urna fringilla ultrices. Phasellus eu tellus sit amet tortor gravida placerat. Integer sapien est, iaculis in, pretium quis, viverra ac, nunc. Praesent eget sem vel leo ultrices bibendum. Aenean faucibus. Morbi dolor nulla, malesuada eu, pulvinar at, mollis ac, nulla. Curabitur auctor semper nulla. Donec varius orci eget risus. Duis nibh mi, congue eu, accumsan eleifend, sagittis quis, diam. Duis eget orci sit amet orci dignissim rutrum.

Nam dui ligula, fringilla a, euismod sodales, sollicitudin vel, wisi. Morbi auctor lorem non justo. Nam lacus libero, pretium at, lobortis vitae, ultricies et, tellus. Donec aliquet, tortor sed accumsan bibendum, erat ligula aliquet magna, vitae ornare odio metus a mi. Morbi ac orci et nisl hendrerit mollis. Suspendisse ut massa. Cras nec ante. Pellentesque a nulla. Cum sociis natoque penatibus et magnis dis parturient montes, nascetur ridiculus mus. Aliquam tincidunt urna. Nulla ullamcorper vestibulum turpis. Pellentesque cursus luctus mauris.

Acknowledgements

Lorem ipsum dolor sit amet, consectetuer adipiscing elit. Ut purus elit, vestibulum ut, placerat ac, adipiscing vitae, felis. Curabitur dictum gravida mauris. Nam arcu libero, nonummy eget, consectetuer id, vulputate a, magna. Donec vehicula augue eu neque. Pellentesque habitant morbi tristique senectus et netus et malesuada fames ac turpis egestas. Mauris ut leo. Cras viverra metus rhoncus sem. Nulla et lectus vestibulum urna fringilla ultrices. Phasellus eu tellus sit amet tortor gravida placerat. Integer sapien est, iaculis in, pretium quis, viverra ac, nunc. Praesent eget sem vel leo ultrices bibendum. Aenean faucibus. Morbi dolor nulla, malesuada eu, pulvinar at, mollis ac, nulla. Curabitur auctor semper nulla. Donec varius orci eget risus. Duis nibh mi, congue eu, accumsan eleifend, sagittis quis, diam. Duis eget orci sit amet orci dignissim rutrum.

Nam dui ligula, fringilla a, euismod sodales, sollicitudin vel, wisi. Morbi auctor lorem non justo. Nam lacus libero, pretium at, lobortis vitae, ultricies et, tellus. Donec aliquet, tortor sed accumsan bibendum, erat ligula aliquet magna, vitae ornare odio metus a mi. Morbi ac orci et nisl hendrerit mollis. Suspendisse ut massa. Cras nec ante. Pellentesque a nulla. Cum sociis natoque penatibus et magnis dis parturient montes, nascetur ridiculus mus. Aliquam tincidunt urna. Nulla ullamcorper vestibulum turpis. Pellentesque cursus luctus mauris.

Contents

Declaration iii

Abstract v

Acknowledgements vii

Abbreviations xi

List of Figures xiii

1 Monte Carlo radiation transport technique 1
- 1.1 Introduction and Background 1
  - 1.1.1 Monte Carlo method 1
- 1.2 Monte Carlo radiation transport algorithm 3
  - 1.2.1 Introduction & background 3
    - 1.2.1.1 Radiative transfer 3
  - 1.2.2 MCRT algorithm 7
    - 1.2.2.1 Medium set-up 7
    - 1.2.2.2 Initialise photon 7
    - 1.2.2.3 Grid set-up 7
    - 1.2.2.4 Photon launch 8
    - 1.2.2.5 Photon move 9
    - 1.2.2.6 Photon scatter and absorbing 10
    - 1.2.2.7 Termination 10
  - 1.2.3 Code details 10
- 1.3 Validation of MCRT code 10
- 1.4 Optical properties 10
  - 1.4.1 Scattering 10
  - 1.4.2 Anisotropy 11
  - 1.4.3 Absorption 12
  - 1.4.4 Other parameters 12
- 1.5 Further extensions to the code 14
  - 1.5.1 Fresnel reflections & refractions 14
  - 1.5.2 Parallelisation of the Monte Carlo radiation Transfer (MCRT) algorithm 14
- 1.6 Improving the voxel tissue model 15

2 Computational modelling of tissue ablation 17
- 2.1 Introduction and background 17
- 2.2 Methods 18

2.2.1 Monte Carlo radiation transport (MCRT) 18
2.2.2 Heat transport 19
2.2.3 Tissue Damage 26
2.2.3.1 Introduction 26
2.2.3.2 Modelling coagulation damage 26
2.2.3.3 Modelling physical tissue damage 27
2.2.4 Validation 28
2.2.4.1 Heat transport validation 28
2.2.4.2 MCRT & heat transport validation 29
2.3 *In silco* results 30
2.3.1 Introduction 30
2.3.1.1 Optical & thermal properties 31
2.3.1.2 Computational speed up: 32
2.3.2 Results 32
2.3.2.1 Investigating ablation temperature, T_a 32
2.3.2.2 Investigating beam type 33
2.3.2.3 Investigating thermal damage 33
2.4 Conclusion 38

Appendix A Heat equation derivation **41**

Abbreviations

T_a ablation temperature.

AMR adaptive mesh refinement.

FDM finite difference method.

K-M theory Kubelka-Munk Theory.

MCRT Monte Carlo radiation Transfer.
MPI Message-passing interface.

OCT optical coherence tomography.

PDF probability density function.
PDT photo-dynamic therapy.

RTE radiative transfer equation.

List of Figures

1.1 Sample buffon needle experiment. 100 needles are dropped on a 10 by 10 cm area with lines spaced 1.5cm apart. If a needle lands on a line it is recorded and coloured blue, else it is yellow. This simulation gave a value of pi as 3.17.

1.2 Computer generated imagery using ray-tracing. Code usd to create image available at: `https://github.com/lewisfish/RayTran`

1.3 Energy flow through area dA within solid angle $d\Omega$ in a direction $\hat{s}$. Adapted from [16, 17]

1.4 Cylindrical volume element, $ds \cdot dA$, with solid angle $d\Omega$ in direction $\hat{s}$ and solid angle $d\Omega'$ in direction $\hat{s}'$. Energy flowing through this element is used to derive the radiative transfer equation (RTE). Adapted from [16, 17].

1.5 blah

1.6 Figure show the g factor for the Henyey-Greenstein phase function, for various configurations of back, forward or isotropic scattering.

1.7 Spectra of some of the more common absorbers found in the skin [27, 31–39].

2.1 Flowchart of the tissue ablation algorithm.

2.2 Red lines are packet paths within a voxel. Black lines packet paths out with the voxel. Red packet paths, weighted by μ_a, are summed up in order to calculate the absorbed energy within each voxel.

2.3 Discretisation of f(x).

2.4 Finite difference method stencil for simple explicit scheme

2.5 Computational domain decomposition. Total computational domain (red outline) is evenly divided between cores in the CPU. This is done via layers of the domain in the z direction. Information is passed to/from cores via the ‘halo swap’ process (see Fig. 2.6).

2.6 Halo swapping. Process A updates the area in red and blue on the left. It updates the blue area which is sent to process B as B’s ‘halo’. Process B cannot update it’s own halo, but rather updates the halo for process A.

2.7 Figure show the speed up gained by parallelisation of the heat simulation using the ‘halo’ swapping technique, for various sizes of computational domain (voxels). Data taken from a Intel Xeon E3-1245 v5, 8 cores @ 3.5GHz machine.

2.8 Ablation of a dog aorta, as viewed under a microscope. Steam vacuoles are clearly visible either side of the ablation area. Carbonisation is also evident at the edges of the ablation fronts. Adapted from [58].

2.9 Comparison between analytical solution and numerical method at t=0.1 s.

2.10 Water absorption coefficient for wavelengths 0-12000nm [33]. Data shows that water is highly absorbing in the infra-red portion of the spectrum compared to the visible portion.

2.11 Simulation of 81 pixel beams. Figure shows a a slice through the optical properties at the end of the simulation. Yellow is unchanged tissue, and purple is completely ablated tissue. Figure shows that the ablation craters do not overlap one another.
2.12 Simulation of 70 W CO_2 ablative laser, with a circular beam profile. Crater depths as a function of pixel beam energy for various ablation temperature (T_a)'s.
2.13 Simulation of 70 W CO_2 ablative laser, with a Gaussian beam profile. Crater depths as a function of pixel beam energy for various T_a's.
2.14 Tissue thermal damage around the ablation crater (white). Thermal tissue damage values of 3 refer to 3^{rd} degree burns, 2 to 2^{nd}, and 1 to 1^{st} degree burns respectively. P is the power in Watts, T_a is the ablation temperature in Kelvin, and E_p is the energy per pixel beam in mJ.
2.15 Figure shows the maximum horizontal extent of thermal damage as a function of energy per pixel beam, for different T_a's.
2.16 Figure show the time taken for 1^{st}, 2^{nd},and 3^{rd} to occur as a function of depth, for a range of T_a's at 400 mJ.
2.17 Figure show the time taken for 1^{st}, 2^{nd},and 3^{rd} to occur as a function of depth, for a range of T_a's at 50 mJ.

Chapter 1

Monte Carlo radiation transport technique

1.1 Introduction and Background

This chapter will provide an overview of the Monte Carlo method and how it is used within the context of MCRT. The chapter will then present the details of the MCRT code used as the basis of the subsequent chapters. Validation of this code and details of computational speed up are also presented. Subsequent chapters will expand upon the code for each individual projects needs.

1.1.1 Monte Carlo method

The Monte Carlo method is a numerical analysis technique based upon random numbers, which are used to calculate unknown variables in problems.

The earliest use of the method is in Buffon's needle experiment of the 18^{th} century [1–3]. Buffon asked the question;

> "Suppose we have a floor made of parallel strips of wood, each the same width, and we drop a needle onto the floor. What is the probability that the needle will lie across a line between two strips?"

The solution to this question is as: for a needle length l, strip separation s, and where x is the distance from the needle to the closest line. Then using a simple geometrical argument, a needle crosses a strip if $x \leq \frac{l}{2} sin\theta$.

x is distributed uniformly in $[0, \frac{s}{2}]$, and θ in $[0, \frac{\pi}{2}]$. Therefore the probability density function for x is $p(x) = \frac{2}{s}$, and θ is $p(\theta) = \frac{2}{\pi}$. The probability density function (PDF), is a function of a variable that gives probability for a variable to a take a given value. The PDF is normalised over the whole range of the variable, in this case x, and θ. Thus, as x and θ are independent variables, giving a joint probability of $p(x, \theta) = \frac{4}{s\pi}$. So the probability of a needle of length l $(l < s)$ is:

$$P = \int_0^{\frac{\pi}{2}} \int_0^{\frac{l}{2} sin\theta} \frac{4}{s\pi} dx d\theta = \frac{2l}{s\pi} \tag{1.1}$$

Equation (1.1) can be used to carry out a Monte Carlo estimation of pi. A simple rearrangement yields: $\pi = \frac{2l}{sP}$ where P is the ratio of needles crossing the line over total number dropped.

Laplace was the first to suggest that Buffon's needle experiment could be used to estimate π [2]. Figure 1.1 shows an example of simulation of Buffon's needle experiment.

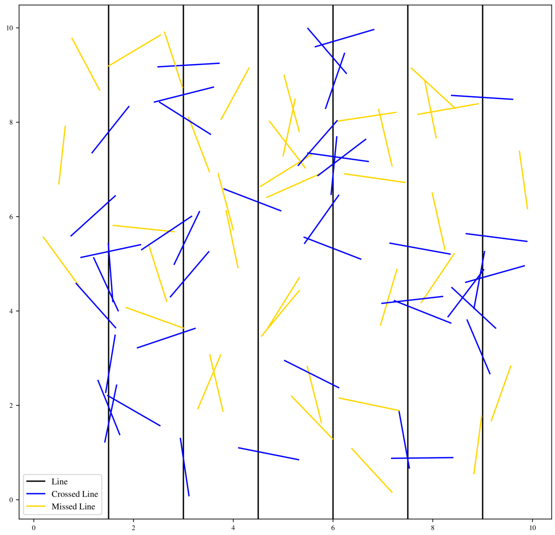

Figure 1.1: *Sample buffon needle experiment. 100 needles are dropped on a 10 by 10 cm area with lines spaced 1.5cm apart. If a needle lands on a line it is recorded and coloured blue, else it is yellow. This simulation gave a value of pi as 3.17.*

The Monte Carlo method is used in various different disciplines. Ranging from use in the financial sector to analyse investments and stocks by simulating the sources of uncertainty which affect their values [4,5], use in statistical analysis [6], and in modern computer generated images (see Fig. 1.2) [7,8]. It is also widely used in astronomy and medicine, in order to simulate the propagation of particles through turbid media. This technique, Monte Carlo radiation transfer, is what makes up the bulk of this thesis and is described in depth in the following sections.

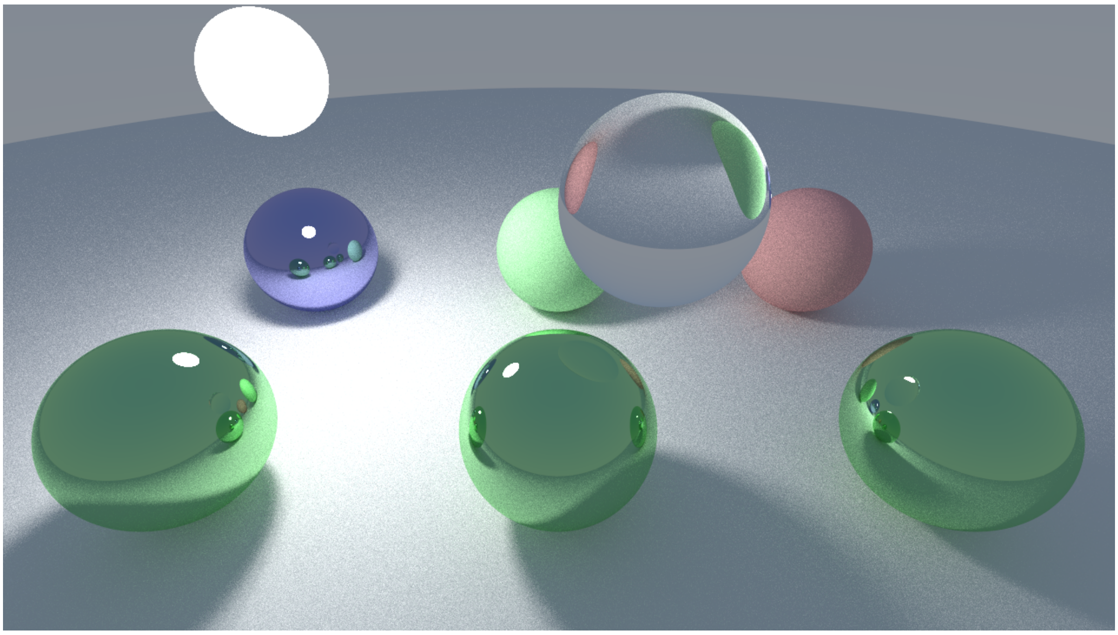

Figure 1.2: *Computer generated imagery using ray-tracing. Code usd to create image available at:* `https://github.com/lewisfish/RayTran`

1.2 Monte Carlo radiation transport algorithm

1.2.1 Introduction & background

The technique that makes up the bulk of this thesis, is the MCRT technique. This method was developed at the tail end of the Second World War at the Los Alamos National Laboratory, for the purpose of calculating neutron diffusion though shielding material [9–12]. It has since found a myriad of applications from light transport through dusty clouds [13], calculating doses for radiotherapy [14] to light transport through tissue [15].***more here + link to next section***

1.2.1.1 Radiative transfer

Transport of photons through turbid media, can be modelled analytically using the RTE. The RTE models the the radiative losses, and gains by a beam of radiation as it travels through a medium, including: loss of energy due to absorption, loss/gain of energy due to scattering, and energy gain due to emission. Before we derive the RTE, we first define some terms and physical quantities.

The first term is spectral irradiance, L_ν. Spectral irradiance is defined as the energy flow in a direction $\mathbf{n}$, for a solid angle $d\Omega$, per unit time per unit temporal frequency bandwidth. Irradiance is defined as the spectral irradiance over a small frequency range $[\nu, \nu + \Delta\nu]$:

$$L(\vec{r}, \hat{s}, t) = L_\nu(\vec{r}, \hat{s}, t)\Delta\nu \tag{1.2}$$

Where:
$\vec{r}$ is the position;
$\hat{s}$ is the unit normal vector;

t is the time;
and $L(\vec{r}, \hat{s}, t)$ is the irradiance $[W \cdot m^{-2} \cdot sr^{-1}]$.

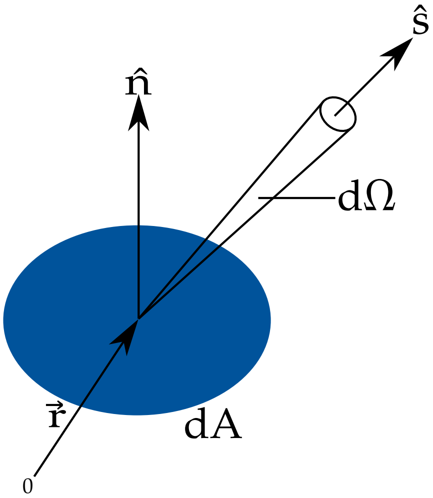

Figure 1.3: *Energy flow through area dA within solid angle $d\Omega$ in a direction $\hat{s}$. Adapted from [16, 17]*

The irradiance can be used to determine the energy, dE, transported across an area dA, in a solid angle $d\Omega$ in a time dt (see Fig. 1.3) is:

$$dE = L(\vec{r}, \hat{s}, t) \cdot (\hat{s} \cdot \hat{n})\ dAd\Omega dt \tag{1.3}$$

Where:
$\hat{n}$ is the unit normal to dA;
and $\hat{s} \cdot \hat{n}$ is the angle of the solid angle.

Irradiance can also be used to determine the fluence rate, ϕ, which is defined as the energy flow per unit time, independent of the flow direction.

$$\phi(\vec{r}, t) = \int_{4\pi} L(\vec{r}, \hat{s}, t)\ d\Omega \tag{1.4}$$

Where:
ϕ is the fluence rate $[W \cdot m^{-2}]$.

Irradiance is also the main variable in the RTE, as it describes the light distribution throughout the medium, and by solving the RTE yields the irradiance, which in turn gives information on the state of the system and all the physical properties of it.

With the irradiance defined, as well as the other quantities that follow, we can now derive the RTE [16, 17]. We first consider conservation of energy, as shown in Eq. (1.5).

$$dP = -dp_{div} - dp_{ext} + dP_{scatt} + dP_{src} \tag{1.5}$$

Where:
dP is the total change in energy in the volume $dAds$ within the solid angle, $d\Omega$, per unit time (see Fig. 1.4);
dP_{div} is the energy loss due to the divergence of the radiation beam per unit time;

dP_{ext} is the energy loss due to absorption and scattering within $dAdsd\Omega$;
dP_{scatt} is the energy gain due to scattering from $\hat{s}'$ into $d\Omega$ per unit time;
and dP_{src} is the energy gain due to emission within the medium, per unit time.

The total change in energy in the volume element within the solid angle $d\Omega$, dP, is equal to:

$$dP = \frac{1}{c}\frac{\partial L(\vec{r}, \hat{s}, t)}{\partial t}\ dAdsd\Omega \tag{1.6}$$

Where c is the speed of light.

The first loss term, dP_{div}, is the energy loss due to divergence of the radiation beam. This is modelled as:

$$\begin{aligned} dP_{div} &= \frac{\partial L}{\partial s}\ d\Omega dV \qquad (1.7)\\ &= \hat{s} \cdot \nabla L(\vec{r}, \hat{s}, t)\ d\Omega dV \qquad (1.8)\end{aligned}$$

dP_{ext} is the second loss term, and accounts for energy loss due to scattering and absorption in the volume element within the solid angle $d\Omega$. This is modelled as:

$$dP_{ext} = \mu_t ds\ L(\vec{r}, \hat{s}, t)\ dAd\Omega \tag{1.9}$$

The first energy gain term, dP_{src}, is due to emission in the volume element within the solid angle $d\Omega$.

$$dP_{src} = S(\vec{r}, \hat{s}, t)\ dVd\Omega \tag{1.10}$$

The second energy gain term, and final term, is due to the incident energy on the volume element within the solid angle $d\Omega$ in direction $\hat{s}$ due to scattering from any direction $\hat{s}'$.

$$\begin{aligned} dP_{scatt} &= N_s dV \left(\int_{4\pi} L(\vec{r}, \hat{s}', t) P(\hat{s}', \hat{s}) \sigma_s\ d\Omega' \right)\ d\Omega \qquad (1.11)\\ &= \mu_s dV \left(\int_{4\pi} L(\vec{r}, \hat{s}', t) P(\hat{s}', \hat{s})\ d\Omega' \right)\ d\Omega \qquad (1.12)\end{aligned}$$

Where:
N_s is the number density of scatters;
$P(\hat{s}', \hat{s})$ is the scattering phase function (see Section 1.4 for further discussion);
and σ_s is the cross section of the scatters, thus $\mu_s = N_s\sigma_s$ (again see Section 1.4 for further discussion).

Finally substituting Eqs. (1.6), (1.8) to (1.10) and (1.12) into Eq. (1.5) yields the RTE:

$$\frac{1}{c}\frac{\partial L(\vec{r}, \hat{s}, t)}{\partial t} + s \cdot \nabla L(\vec{r}, \hat{s}, t) = -\mu_t L(\vec{r}, \hat{s}, t) + \mu_s \int_{4\pi} p(\hat{s}, \hat{s}') L(\vec{r}, \hat{s}', t) d\Omega' + S(\vec{r}, \hat{s}, t) \tag{1.13}$$

In general, the RTE is hard to solve in arbitrary 3D geometries, however there are a number of approximations, and numerical methods available. Diffusion approximation, Kubelka-Munk Theory (K-M theory), and MCRT are the common methods used to approximate the RTE.

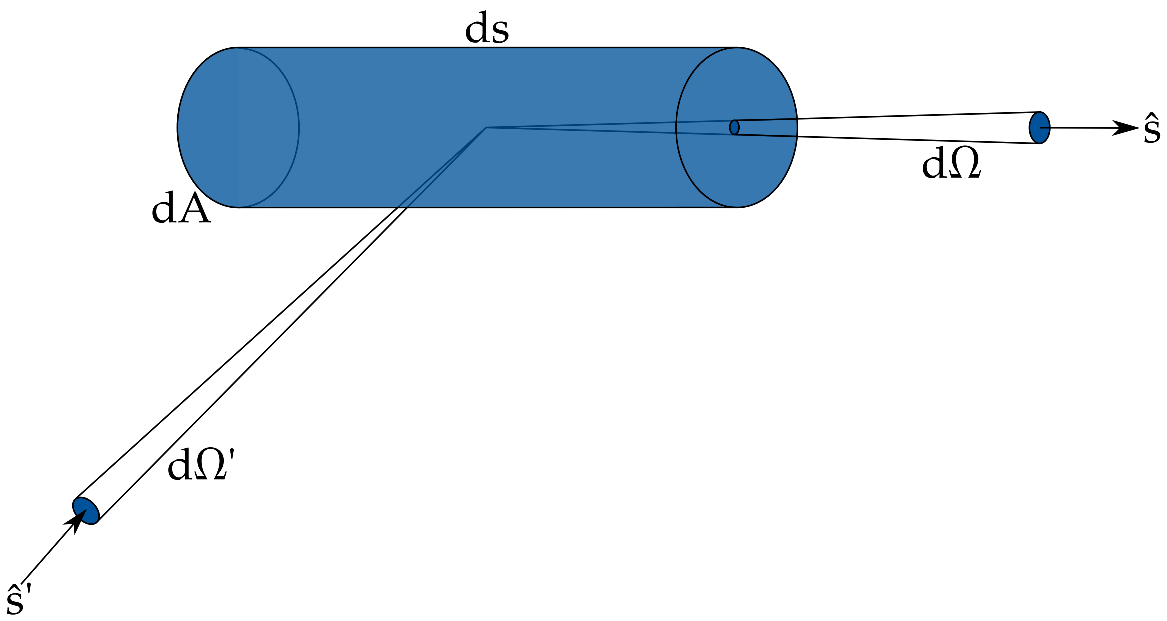

Figure 1.4: *Cylindrical volume element,* $ds \cdot dA$*, with solid angle* $d\Omega$ *in direction* $\hat{s}$ *and solid angle* $d\Omega'$ *in direction* $\hat{s}'$*. Energy flowing through this element is used to derive the RTE. Adapted from [16, 17].*

Kubelka-Munk theory K-M theory was originally developed in order to calculate the light distribution in thin layered materials, such as paint or paper [18]. The theory is rather simple and makes many assumptions about the medium and the incident light. The main assumptions of K-M theory are: only scattering and absorption take pace in the medium, the incident light is already diffuse, the medium is uniform, only isotropic scattering, no external or internal reflections, and the medium is planar and infinitely wide [19–21].

These assumptions make K-M theory, very poor for modelling light-tissue interactions. This is as in tissue, scattering is not isotropic, but rather forward biased (see Section 1.4). Tissue is rarely, if ever, planar and infinitely wide. Tissue also has some reflections at its external and internal boundaries, due to change in refractive indices. Many medical and biophotonic treatments/methods use laser light which is not diffuse. Finally tissue can also exhibit fluorescence, which K-M theory is not able to model, along with polarization. K-M theory does have some positive aspects. It is good at calculating the diffuse reflectance of simple mediums, and can be used to roughly estimate calculations. Though it is not well suited for modelling light-tissue applications.***refs for these claims***

Diffusion approximation The diffusion approximation for the RTE, is where the irradiance is separated into two components:

$$L(\vec{r}, \hat{s}) = L_c(\vec{r}, \hat{s}) + l_d(\vec{r}, \hat{s}) \tag{1.14}$$

Where L_c is the unscattered contribution, which satisfies Beer's law[*], and L_d is the diffuse contribution. The L_d component is expanded using Legendre polynomials and truncated. The diffusion approximation also has a number of assumptions and restrictions. The main assumption is that scattering dominates over absorption, and that the scattering is nearly isotropic. This restricts the types of scattering the Diffusion approximation can model, though using similarity relations can partially model scattering in tissue [22, 23].

---

[*] Beer's law (or Beer-Lambert law) states that the transmission, T, is equal to $e^{-\mu L}$, where L is the distance and μ is the attenuation coefficient.

Diffusion theory is computationally fast, and simple. However it is poor at modelling light-tissue interactions due to it's assumptions and restrictions, mainly the inaccurate modelling near the boundaries of the medium and its lack of modelling fluorescence and other microphysics. However it can be used to speed up MCRT in optically thick regions [24, 25].

The final method, MCRT, is a method that is numerically equivalent to the RTE [16]. MCRT is a very flexible method, it can model arbitrary 3D geometries, various microphysics: fluorescence, and polarisation. It can also model various different light sources, from collimated laser beams, to diffuse light sources. The only downside that is noted in the literature is that the MCRT can be very expensive computationally. However with computational power growing faster with each year, this is less and less of a problem going forward. The next several sections give an in depth description of the MCRT method and it's flexibility, along with a description of the code used in this thesis to solve various medical and biophotonic problems.

1.2.2 MCRT algorithm

The MCRT algorithm can be as simple as a ~ 20 line program to as complex as needed for the problem at hand. This section will provide an in depth description of the MCRT algorithm (see also Fig. 2.1). The following section will provide details of how the MCRT algorithm is implemented in the Fortran programming language, along with the various code details, such as the implementation of the 3D voxelised medium.

1.2.2.1 Medium set-up

The first step of any MCRT algorithm , is to set-up the medium the photons will propagate through. There are a variety of ways that the medium can be set-up, for this section, we will assume the medium is an isotropic sphere, radius R, and centred at the origin. for simplicity we will only consider one wavelength, λ. The following section will detail arbitrary geometries and cases where there are more than one wavelength of interest.

1.2.2.2 Initialise photon

The second step in the MCRT algorithm, is to initialise the photon. Initialisation of the photon involves setting its initial position and direction. Again how this is done depends on the experiments being simulated. Here we initialise the photon to the centre of the sphere. The initial direction is sampled isotropically, and set accordingly:

$$n_x = sin(\theta) \cdot cos(\phi) \tag{1.15}$$

$$n_y = sin(\theta) \cdot sin(\phi) \tag{1.16}$$

$$n_z = cos(\theta) \tag{1.17}$$

With θ and ϕ sampled uniformly between $[0, acos(2\xi - 1)]$ and $[0, 2\pi\xi]$ respectively.

1.2.2.3 Grid set-up

The first step of the MCRT algorithm is to set-up the grid which acts as the simulated medium. This grid consists of $n \times n \times n$ voxels[†] of which each voxel has it's own optical properties (see Section 1.4 for discussion). This allows the medium of interest to be discretised onto a grid, which gives a good approximation of the real-life medium (see Section 1.5 for discussion on this). along with setting up the medium, arrays which store the locations of the voxel walls in each cardinal direction are created for reference in later parts of the code. Once the medium has been set-up photon packets are launched and propagated through the voxel structure.

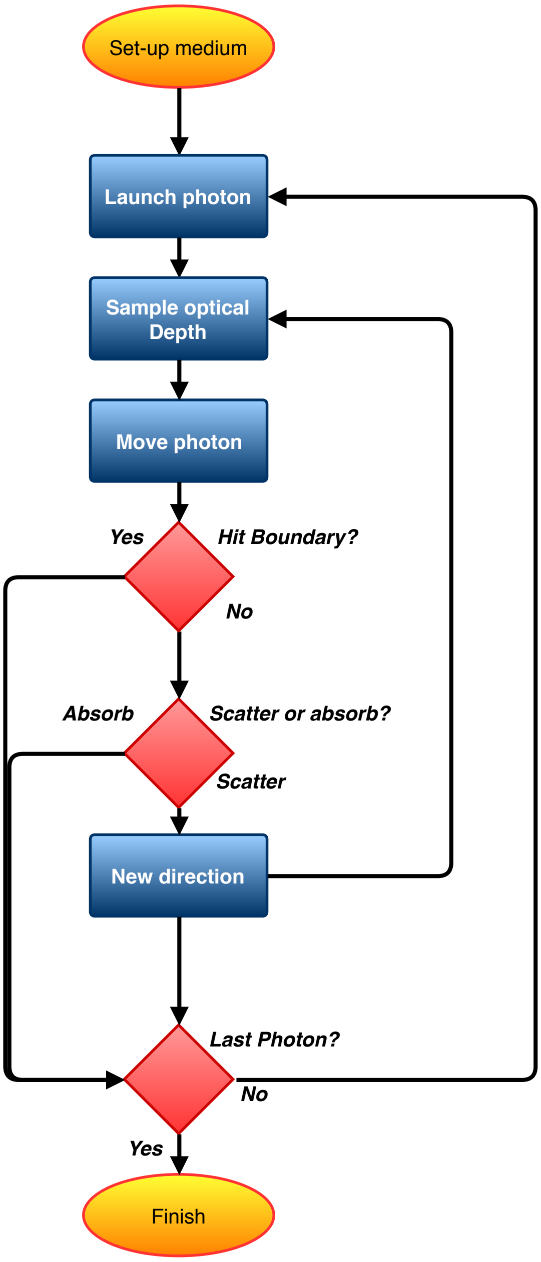

Figure 1.5: *blah*

1.2.2.4 Photon launch

The initial step (besides medium set-up and other book keeping) of any MCRT algorithm is to launch a photon packet. Depending on the source of photon packets for a given simulation, this step varies from simulation to simulation. The general idea of launching a photon packet is that the packet is given an initial direction vector and position (which consists of a physical position and a voxel position)[‡]:

$$direction = \begin{bmatrix} n_{xp} \\ n_{yp} \\ n_{zp} \end{bmatrix} \tag{1.18}$$

$$position = [x_p, y_p, z_p] \tag{1.19}$$

$$voxel = [x_{cell}, y_{cell}, z_{cell}] \tag{1.20}$$

In order to set the direction vectors, the components of the direction vectors must be first set. The packets position is tracked using a Cartesian coordinate system, however for ease of computation for calculating scattering angles (see Section 1.2.2.6), the direction vectors are computed in a spherical system thus the direction vectors are:

$$n_{xp} = sin(\theta) \cdot cos(\phi) \tag{1.21}$$

$$n_{yp} = sin(\theta) \cdot sin(\phi) \tag{1.22}$$

$$n_{zp} = cos(\theta) \tag{1.23}$$

[†] A voxel is a 3D pixel

[‡] all variables given in this section are the same as they are in the code.

θ and ϕ are generated dependant on the photon source used. The individual sine and cosine terms are saved for use in the scattering routines, see Section 1.2.2.6.

1.2.2.5 Photon move

The next step in the algorithm is moving a packet to the next interaction point. The probability a packet will interact over a distance dL is $\mu_t dL$, where μ_t is the interaction probability (see Section 1.4). Thus the probability of travelling dL without any interaction is $1 - \mu_t dL$. Therefore over a distance L, with N segments of length L/N the probability of travelling L before any interaction:

$$P(L) = (1 - \mu_t \frac{L}{N}) \cdot (1 - \mu_t \frac{L}{N}) ... (1 - \mu_t \frac{L}{N}) = (1 - \mu_t \frac{L}{N})^N \tag{1.24}$$

$$P(L) = \lim_{N \to \infty} (1 - \mu_t \frac{L}{N})^N = e^{-\mu_t L} = e^{-\tau} \tag{1.25}$$

Where τ is the number of mean free paths over a distance L. We now have a PDF, Eq. (1.25), for the distance a packet will travel before an interaction occurs. For this to be of use we need to be able to sample from this PDF in order to get a random optical depth. Using the Monte Carlo method described in Section 1.1.1, with ξ as our random variable, we get:

$$\xi = \int_0^\tau e^{-\tau'} = 1 - e^{-\tau} \rightarrow \tau = -log(1 - \xi) \tag{1.26}$$

As ξ is symmetric about 0.5 we can substitute $1 - \xi$ for ξ yielding:

$$\tau = -log(\xi) \tag{1.27}$$

We now have an optical distance, however we need to convert this into a physical distance so that we can move our photon packet. From our definition of τ we know that $\tau = \int_0^L \mu_t dS$, and if we have a smooth, homogeneous medium (i.e not a gridded medium) thus

$$L = \frac{\tau}{\mu_t} \tag{1.28}$$

Therefore in order to update the packets position is simply:

$$x_p = x_p + L \cdot n_{xp} \tag{1.29}$$

$$y_p = y_p + L \cdot n_{yp} \tag{1.30}$$

$$z_p = z_p + L \cdot n_{zp} \tag{1.31}$$

However as the code in this thesis is a 3D gridded Cartesian code, we have to slightly adjust how we move and update the packets position. As stated in Section 1.2.2.3, the medium has been discretised onto a grid, so that each voxel can have a different μ_t, thus Eq. (1.28) becomes:

$$L = \frac{\tau}{\mu_{t,\zeta}} \qquad \zeta = (x, y, z) \tag{1.32}$$

with $\mu_{t,\zeta}$ the μ_t for the ζ^{th} voxel. The position is then updated as before using Eqs. (1.29) to (1.31). The next step in the algorithm is the interaction event, which can consist of either: scattering, absorbing or fluorescing.

1.2.2.6 Photon scatter and absorbing

The first part of this section of the algorithm is to decide what kind of interaction the packet has with the medium. This section will focus on scattering and absorbing with other interaction events left for the chapters that detail these behaviours.

To decide whether a packet scatters or absorbs involves ‘throwing’ a random number and comparing it against the albedo. As detailed in Section 1.4 the albedo is the scattering probability $a = \frac{\mu_a}{\mu_a+\mu_s}$. The random number is compared to the albedo, and if the random number is less than the albedo then the packet scatters, otherwise the packet is absorbed.

Packet absorption

If the interaction event is a photon packet absorption, then the algorithm terminates the photon packets and starts the next photon packet, Section 1.2.2.7.

Packet scattering

If the interaction event is a packet scattering, then the packet is scattered into a new direction and the above process are carried out until a termination clause is met, see Section 1.2.2.7.

Depending of the medium being simulated, it can either be isotropically scattering or preferentially scattering in a direction. In the case of simulating photon propagation in tissue, tissue is highly forward scattering.

Anisotropy is the degree of deviation in the photon packets path at each interaction event. The measure of anisotropy is the g value, g. With g taking any value from -1 to 1, -1 is highly backward scattering, 0 is isotropic scattering and 1 is highly forward scattering.

1.2.2.7 Termination

1.2.3 Code details

This section details the the actual implementation of the MCRT algorithm detailed in the previous section, along with any computational necessities and speed ups on the original algorithm.

1.3 Validation of MCRT code

1.4 Optical properties

Optical properties of a medium are the properties that determine how light is transported though that medium. Usually the optical properties of a medium are defined by three main parameters: the scattering and absorption coefficients (μ_s and μ_a), and the anisotropy coefficient (g). There are several other optical properties the medium can be defined with, however these in general are only used for specific applications, such as Raman cross-sections for Raman scattering.

1.4.1 Scattering

The scattering coefficient, along with the anisotropy value (see Section 1.4.2), define how light is scattered in a medium. Scattering occurs in skin due to a number of different scatterers, and inhomogeneities found within the skin. The main scatters in the skin are filamentous proteins such as collagen and elastin. These proteins are generally found within the dermis and epidermis [26]. In the upper layers of the skin, the main scatters are keratins and various chromophores such as melanin. The size of the aforementioned scatters affect how light is scattered and into which direction that light is scattered into.

The scattering of light within tissue is usually defined as μ_s or μ_s': the scattering coefficient and the reduced scattering coefficient, where $\mu_s' = \mu_s(1-g)$. The scattering coefficient is defined such that the probability of transmission without scattering in a path length L is:

$$T = e^{-\mu_s L} \tag{1.33}$$

This gives units of inverse length for the scattering coefficient (usually measured in cm^{-1}). The reduced scattering coefficient is quite often given in place of the scattering coefficient, as the reduced coefficient is more easily measured then the 'normal' coefficient [27].

1.4.2 Anisotropy

Anisotropy is the degree of deviation that light undergoes at each scattering event. The anisotropy value is taken from the phase function for the medium. The phase function, $\Phi(\theta, \phi)$, is usually normalised over all angles:

$$\int_\Omega \Phi(\theta, \phi)\ d\Omega = 1 \tag{1.34}$$

Where θ, and ϕ are the usual spherical angles. Thus the usual Rayleigh scattering and isotropic scattering, phases function's are:

$$\Phi_{isotropic}(\theta, \phi) = \frac{1}{4\pi} \tag{1.35}$$

$$\Phi_{Rayleigh}(\theta, \phi) = \frac{3}{8\pi}(1 + cos^2(\theta)) \tag{1.36}$$

For simplicity, the phase function is usually cast as the anisotropy value g, which is defined as the average angle of deflection:

$$g = \langle cos(\theta) \rangle = \int_\Omega cos(\theta)\Phi(\theta, \phi)\ d\Omega \tag{1.37}$$

The anisotropy factor, g, can take on any value from -1 to 1. Where a value of -1 is highly back scattering, 0 is isotopic scattering, and 1 is highly forward scattering.

There are many phase functions that can be used to model the anisotropy factor in a medium. the standard phase function in biological tissue is the Henyey-Greenstein phase function. The Henyey-Greenstein phase function, was originally created to modelling diffuse radiation in the galaxy [28, 29]. The Henyey-Greenstein phase function has become the *de-facto* phase function for biological tissue. This is due to the phase functions, relative simplicity and due to it being regarded as a 'good' phase function for accurately modelling scattering in biological tissue [30]. The Henyey-Greenstein phase function is shown in Eq. (1.38):

$$\Phi_{H.G}(\theta, \phi) = \frac{1}{4\pi}\frac{1 - g^2}{(1 + g^2 - 2g\ cos(\theta))^{\frac{3}{2}}} \tag{1.38}$$

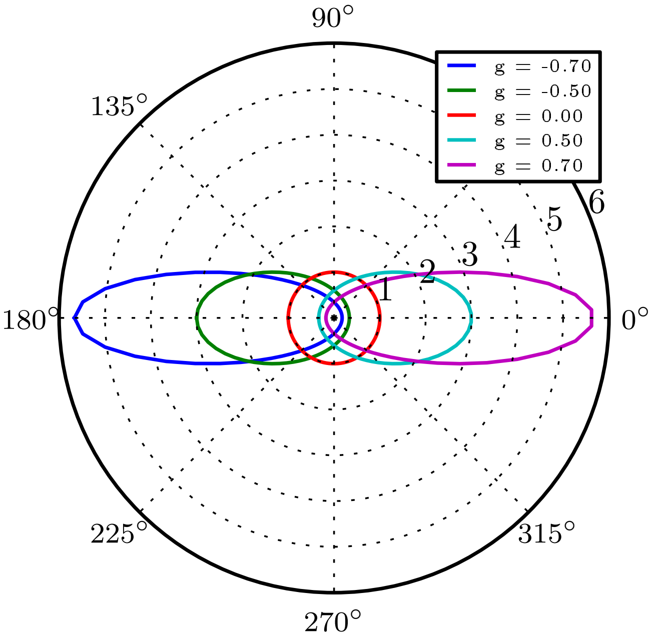

Figure 1.6: *Figure show the g factor for the Henyey-Greenstein phase function, for various configurations of back, forward or isotropic scattering.*

1.4.3 Absorption

Absorption of light by a medium is defined by the absorption coefficient μ_a. The absorption coefficient is defined, as before with the scattering coefficient, by considering the probability of transmission without absorbing in a path length L:

$$T = e^{-\mu_a L} \tag{1.39}$$

This, again like the scattering coefficient, gives inverse distance for the unit of the absorption coefficient (and its is also usually measured in units of cm^{-1}).

There are various sources of absorbers in tissue: blood, water, fat, melanin, β-carotene, bilirubin are among the more absorbing chromophores. These chromophores can all contribute, depending on the probing wavelength, with some more absorbing than others, see Fig. 1.7.

1.4.4 Other parameters

The preceding subsection, described the optical properties that this thesis will use in every chapter. However there are other optical properties that can be used to define a medium. These other parameters generally are used to model microphysics such as Raman scattering, polarization, fluorescence or reflection/refraction. This section will give a brief overview of these other optical properties.

Refractive index The refractive index of a medium, defines how fast light propagates through that medium. Generally for tissue, the refractive index is given as a bulk refractive index.

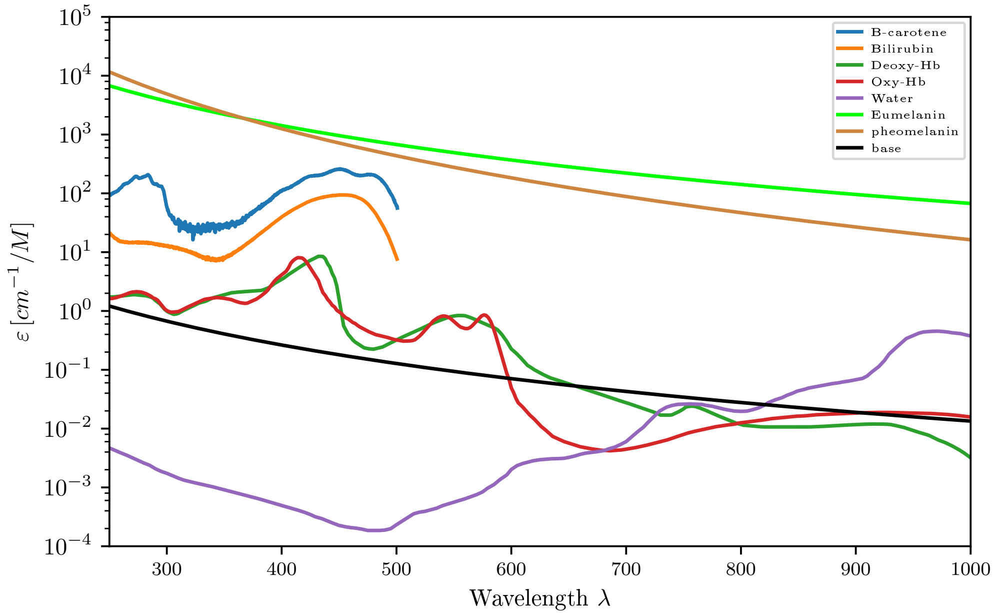

Figure 1.7: *Spectra of some of the more common absorbers found in the skin [27, 31–39].*

Meaning that the medium is divided into sections, with each section given a refractive index. For example, skin's refractive indices are divided up by the different layers of skin (as shown in Table 1.1).

Layer	**Refractive index**
Stratum Corenum	1.53
Epidermis	1.34
Papillary Dermis	1.395
Reticular Dermis	1.39
Hypodermis	1.44

Table 1.1: *Example of refractive indices per layer of skin for a λ=632.8 nm [40].*

Details on how refraction is implemented with the code can be found in ***ref here***.

Raman Scattering Raman scattering is where a photon is scattered inelastically, which excites the molecule the photon scattered off, thus decreasing the energy of the photon and increasing the photons wavelength. The optical property needed to model Raman scattering, is the Raman scattering cross section. The cross section, like the absorption or scattering coefficient, is the likelihood of a photon undergoing a Raman scattering event. Raman scattering has been modelled in MCRT in order to simulate spatially offset Raman spectroscopy for breast tumour analysis [41].

Fluorescence Fluorescence occurs when a photon is absorbed by a fluorescent molecule and re-emitted with a new wavelength. Fluorescence is a reactively common phenomena, and is heavily utilised in biophotonics and medicine, in order to image, or monitor molecules in tissue. Again the optical property that models fluorescence is coefficient that gives the probability of absorption and re-emission of a photon by a certain molecule. Usually this is in the form of an absorption coefficient or extinction coefficient. The extinction coefficient is a measurement of absorption in terms of the concentration of that absorber. Thus if a medium has many fluorophores, then the total absorption coefficient is the bulk absorption of the medium plus the contribution from the fluorophores as in Eq. (1.40):

$$\mu_a = ln10 \sum_i C_i \varepsilon_i \tag{1.40}$$

Fluorescence will be described in more depth in **??**??.

1.5 Further extensions to the code

This section details the miscellaneous additions to the MCRT algorithm that the various chapters in this thesis may or may not use.

1.5.1 Fresnel reflections & refractions

this section in madrid work?

$$R_s = \left| \frac{n_1 \; cos\theta_i - n_2 \; cos\theta_t}{n_1 \; cos\theta_i + n_2 \; cos\theta_t} \right|^2 \tag{1.41}$$

$$R_p = \left| \frac{n_1 \; cos\theta_t - n_2 \; cos\theta_i}{n_1 \; cos\theta_t + n_2 \; cos\theta_i} \right|^2 \tag{1.42}$$

1.5.2 Parallelisation of the MCRT algorithm

As mentioned in the previous sections, MCRT can be computationally intensive, especially when dealing with highly scattering mediums. Fluorescence can also cause simulations times to drastically increase as photons are no longer 'killed' off, but rather re-emitted at a new wavelength. Other optical processes such as Raman scattering are highly unlikely events, which again can lead to a dramatic increase in simulation times, as many photons are required to be simulate in order to get 'good' statistics.

Fortunately MCRT is classed as an 'embarrassingly parallel' problem[§]. This means that it is trivial to parallelise in comparison to other algorithms. The reason that MCRT is classed as 'embarrassingly parallel', is that the algorithm can be split up onto separate processes, with no little need for communication between them. In reality this means that n copies of the algorithm can run on n cores in a processor, with communication taking place at the start and end of each simulation run.

All the code in this thesis is parallelised using Message-passing interface (MPI), with the only communication taking place at the end, where the path length estimators are collated on to all process.

ToDO do parallel tests finish writing this subsection ***ToDO***

[§] However this is not true for all MCRT applications. For example using the Bjorkman & Wood [42] immediate temperature corrections method, turns MCRT into a different class of parallel problem [43].

1.6 Improving the voxel tissue model

Needed?

As voxels are cuboid in shape, in order for them to accurately model biological tissue, which is decidedly not smooth, new methods or approximations were attempted to improve the modelling of biological tissue. The first is bump-mapping, a technique borrowed from computer graphics. The second is to dispense with the voxel model and use a triangular based mesh. Both these methods were tried during the course of this thesis, but were abandoned due to time constraints. This section gives a brief overview of these techniques and why they were not ultimately used in this thesis.

Chapter 2

Computational modelling of tissue ablation

2.1 Introduction and background

This chapter uses MCRT techniques coupled to a heat transfer simulation, in order to study the thermal damage to tissue due to fractional lasers. Fractionated ablative lasers are ablative lasers where the power is spread over several beams, to leave viable tissue around zones of damaged/necrotic tissue [44]. We present experimental work carried out on porcine tissue by our collaborators at the University of Dundee and the photobiology department at Ninewells hospital, along side our computational model of tissue ablation.

Ablative lasers are used in a wide variety of medical procedures not limited to: coagulating scalpels, port wine stain removal, tattoo removal, hair removal, and skin rejuvenation [45–49]. One class of laser used in these procedures are ablative lasers. Ablative lasers are usually high powered lasers (>30 W) targeted at a specific chromophore in the skin, to partially or fully remove layers of skin. These types of lasers are commonly used for aesthetic procedures such as: skin rejuvenation [49], and removal of various diseases such as Rhinophyma [50] or lesions/nodules [51]. Ablative lasers have also been recently investigated as a means of better drug penetration into the skin for various therapies such as photo-dynamic therapy (PDT). The ablative laser 'drills' holes in the skin, which allows topical treatments to better diffuse into the skin [52].

One downside to using lasers to remove tissue, is that unlike a scalpel where the surgeon has full control of the depth of the incision, ablative lasers are not as predictable. Lasers can cause thermal damage to the surrounding areas, leading to potentially unwanted effects, though some applications of ablative lasers utilise the thermal damage, particularly aesthetic procedures [53].

Currently the only reliable method to measure the depth of the ablative holes, is via a biopsy, which is an invasive procedure. In this work an optical coherence tomography (OCT) system is used to measure the ablative crater non-invasively *in-vivo*. The OCT measurements are then compared to a computational model developed as part of this project. It is hoped this computational model could be used to predict the depth of the ablative crater when using a certain laser power for various different applications such as: laser assisted drug delivery, and various cosmetic applications.

2.2 Methods

In order to replicate the experimental work *in silico*, the numerical model has three main portions. The first is the MCRT code that models light transport through tissue so that we can calculate the laser energy deposited as a function of time and space. The second, a finite difference method (FDM) which is used to calculate the heat diffusion within the tissue due to the absorbed laser energy. Finally, a tissue damage model to track the tissue damage caused by the laser. All these individual portions are connected together to create our numerical model. This chapter explains in detail each portion of the numerical model used to simulate tissue ablation via a laser.

2.2.1 Monte Carlo radiation transport (MCRT)

MCRT is used here to calculate the energy deposited by the laser. This is then passed to the heat transport simulation, which calculates the heat diffusion in the medium. The algorithm for the the three coupled simulations is presented in Fig. 2.1.

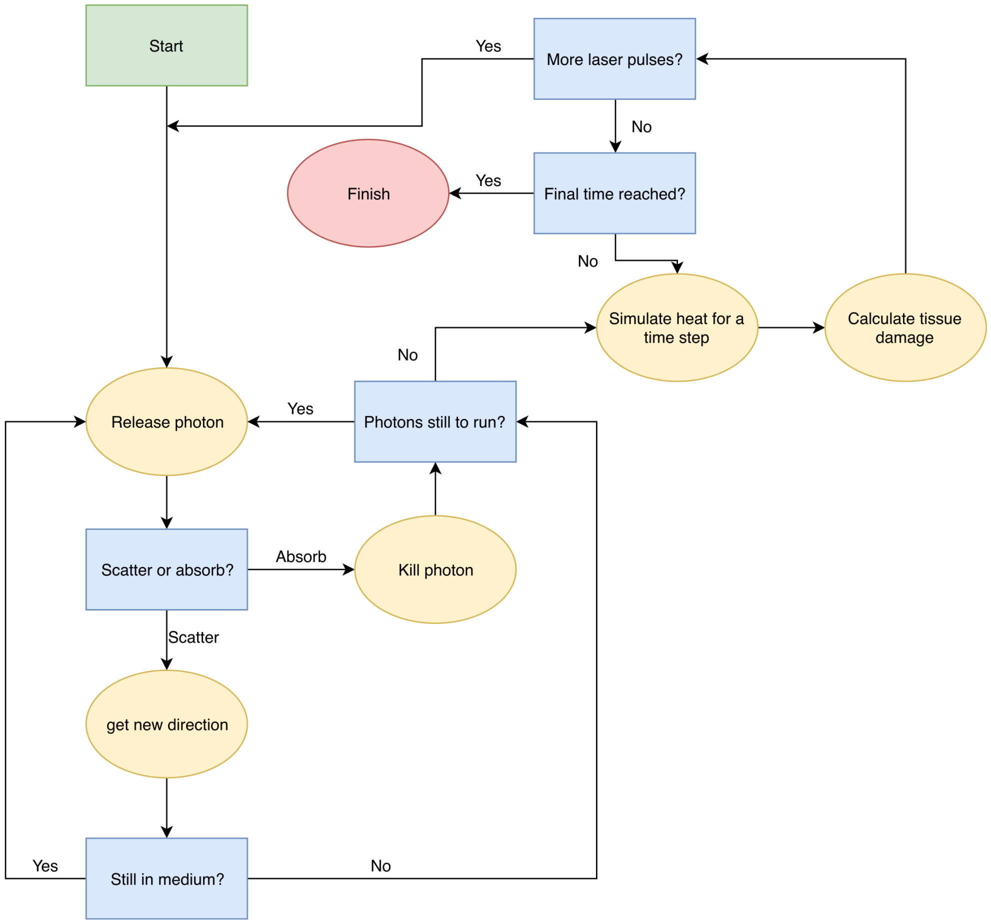
Start
Yes
More laser pulses?
No
Finish
Yes
Final time reached?
No
Simulate heat for a time step
Calculate tissue damage
No
Release photon
Yes
Photons still to run?
Scatter or absorb?
Absorb
Kill photon
Scatter
get new direction
Yes
Still in medium?
No

Figure 2.1: *Flowchart of the tissue ablation algorithm.*

The MCRT algorithm is largely the same as described in Chapter 1, with a couple of key adjustments.

The first adjustment to the algorithm is that the path length counter for fluence is adjusted to track absorbed energy instead. This is achieved by multiplying the pathlength in a voxel by the absorption coefficient of that voxel. Figure 2.2 show this process graphically, and Equation (2.36) shows the mathematical expression:

$$E_i^{abs} = \frac{P}{NV_i}\sum \mu_{a,i} s \tag{2.1}$$

Where:

P is power $[W]$;
N is the number of packets, representing a power, P;
V_i is the volume of the i^{th} voxel $[m^{-3}]$;
$\mu_{a,i}$ is the absorption coefficient of the i^{th} voxel $[cm^{-1}]$;
and s is the pathlength of a packet through the i^{th} voxel $[cm]$.

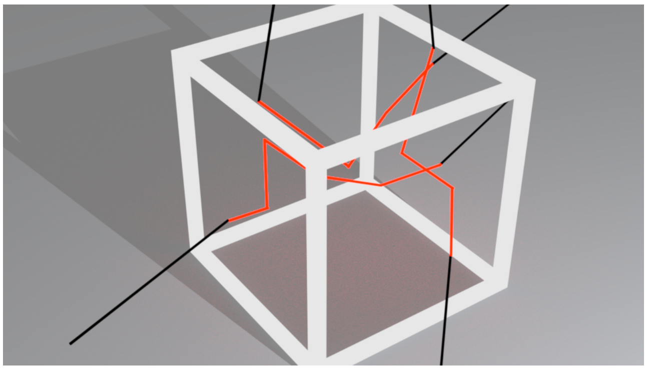

Figure 2.2: *Red lines are packet paths within a voxel. Black lines packet paths out with the voxel. Red packet paths, weighted by μ_a, are summed up in order to calculate the absorbed energy within each voxel.*

This grid of absorbed energy is then passed to the heat transport portion of the simulation, so that the heat diffusion in the porcine tissue can be calculated.

The next adjustment to the MCRT algorithm, is that the MCRT algorithm is run for every heat simulation time step. The simulation needs to be run for every time step, as the medium could change at every time step due to the optical, and thermal properties changing as a function of tissue damage.

Finally, to match the experiment undertaken the medium and laser for the *in-silico* experiments must match the 'real life' experiments. As the laser used in the experiments emits an infra-red wavelength, the optical properties are dominated by the water content of the tissue. Due to this we model just absorbing in the medium, with no scattering. Further discussion of this can be found in Section 2.3.1.1. The laser in some of the *in silico* experiments, has multiple beams. Thus the source photon packet routine is adjusted to accommodate this when needed.

2.2.2 Heat transport

The diffusion of heat can be modelled using the heat equation (Eq. (2.2)), which is derived from Fourier's law and the principle of conservation of energy [54] (see Appendix A). The standard heat equation is a partial differential equation of the parabolic form. Solutions and analytical methods are readily available for lower dimensions (i.e. 1D heat diffusion), but for higher dimensions such as three dimensions, numerical models must be used for all except the simplest problems. The simplest form of the heat equation is shown below:

$$\rho c_p \frac{\partial T}{\partial t} = \nabla \cdot (\kappa \nabla T) + \dot{q} \tag{2.2}$$

Where:
$T(x, y, z, t)$ is the temperature as a function of time and space $[K]$;
κ is the thermal conductivity $[W m^{-1} K^{-1}]$;
ρ is the density $[Kg m^{-3}]$;
c_p the specific heat capacity $[J K^{-1}]$;
$\dot{q}(x, y, z, t)$ is the source/sink term as a function of time and space $[W m^{-3}]$.

Equation (2.2) is for a homogeneous system where the thermal properties do not change as a function of time, space and/or temperature. However in order to model a moving ablation front we must use the non-linear heat equation where the thermal properties can be a function of time, space and/or temperature (Eq. (2.3)).

$$\frac{\partial T}{\partial t} = \frac{1}{(\rho c_p)_\xi} (\nabla k_\xi T + k_\xi \nabla^2 T) + \dot{q} \quad \xi = (i, j, k) \tag{2.3}$$

We have also included in the Eq. (2.3) a source and sink term, $\dot{q}$ to allow the modelling of heat loss/gain from external sources/sinks. The heat source in this simulation is due to the laser, and we assume the only loss of heat to the surrounding medium is via convection and conduction.

All faces of the cube, except the laser facing face, are considered to be pinned at 5°C, as the porcine skin was kept cooled prior to experimental work and the simulation volume is smaller than the porcine tissue samples. The face of the medium on which the laser is incident, has a simple convective BC (based upon Newtons law of cooling):

$$\dot{q}_c = -hA(T - T_\infty) \tag{2.4}$$

Where:
h is the heat transfer coefficient $[W m^{-2} K]$;
A is the area of the grid element, that is radiating/convicting heat away $[m^{-2}]$;
and T, and T_∞ are the temperature in a voxel and the surrounding medium temperature respectively $[K]$.

As Eq. (2.3) is generally hard to solve in arbitrary geometries with complex boundary conditions we employ a numerical method to solve it. The numerical method we employ is a FDM, derived from the Taylor series, see Eq. (2.5).

A function $f(x)$ is discretised onto a grid with N nodes a distance Δx apart (see Fig. 2.3). We can then truncate and rearrange Eq. (2.5) and assume that the remainder term R_1 is sufficiently small enough, to yield an approximation for the first derivative of a function $f(x)$ at a point $x_0 + \Delta x$, see Eq. (2.6). Equation (2.6) is the so called forward difference, due to it using a point in the 'forward' direction. We can also calculate the 'backward' and central difference terms by using a node at $x_0 - \Delta x$ for the backward difference Eq. (2.7b). The central difference (Eq. (2.7c)) is an average of the forward and backwards differences. We can also give expressions for the 2^{nd} derivatives for backward, forward and central (forward and backward 2^{nd} order equations omitted for brevity) Eq. (2.7d).

$$f(x_0 + \Delta x) = f(x_0) + \frac{f'(x_0)}{1!}\Delta x + \frac{f''(x_0)}{2!}\Delta x^2 + ... + \frac{f^{(n)}(x_0)}{n!}\Delta x^n + R_n(x) \tag{2.5}$$

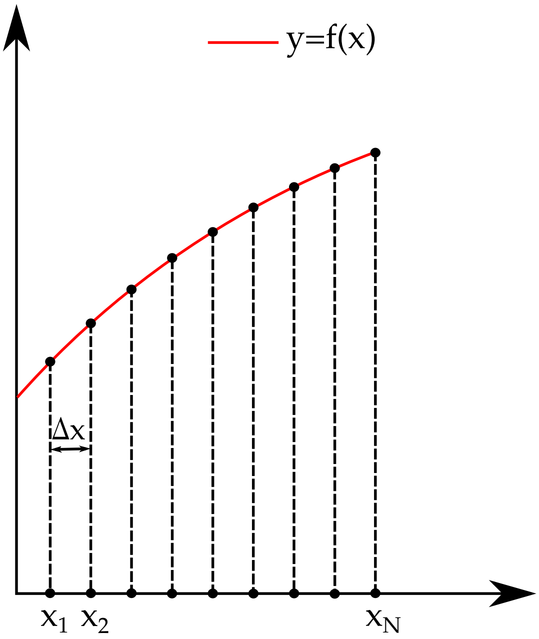

Figure 2.3: *Discretisation of f(x).*

$$f'(x_0) \approx \frac{f(x_0+\Delta x) - f(x_0)}{\Delta x} \tag{2.6}$$

$$\frac{df}{dx} = \frac{f_{i+1} - f_i}{\Delta x}{}^{*} \qquad (forward) \tag{2.7a}$$

$$\frac{df}{dx} = \frac{f_i - f_{i-1}}{\Delta x} \qquad (backward) \tag{2.7b}$$

$$\frac{df}{dx} = \frac{f_{i+1} - f_{i-1}}{2\Delta x} \qquad (central) \tag{2.7c}$$

$$\frac{d^2 f}{dx^2} = \frac{f_{i-1} - 2f_i + f_{i+1}}{\Delta x^2} \qquad (central) \tag{2.7d}$$

Thus the linear heat equation Eq. (2.2), in 1D, taking a 1st order forward time derivative, and a 2nd order central spatial derivative gives:

$$\frac{T_i^{n+1} - T_i^n}{\Delta t} = \alpha \frac{T_{i-1}^n - T_i^n + T_{i+1}^n}{\Delta x^2} + \frac{\dot{q}}{\rho c_p} \tag{2.8a}$$

$$T_i^{n+1} = \alpha \Delta t \frac{T_{i-1}^n - 2T_i^n + T_{i+1}^n}{\Delta x^2} + \frac{\Delta t \dot{q}}{\rho c_p} \tag{2.8b}$$

Where $\alpha = \frac{\kappa}{\rho c}$.

---

[*] For brevity we define $f(x_0 + \Delta x)$ as f_{i+1}, $f(x_0 - \Delta x)$ as f_{i-1}, etc.

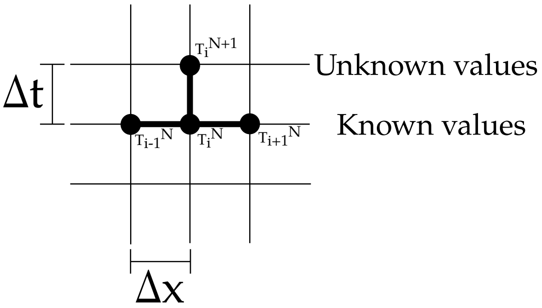

Figure 2.4: *Finite difference method stencil for simple explicit scheme*

Equation (2.8b) is called the ‘simple explicit form of finite-difference approximation’ [55]. Figure 2.4 shows the ‘stencil’ of this scheme, where there are three known points at time N, and just one unknown at time $N+1$. There are various other schemes that can be used to calculate the temperature at the the next time step. However we use a simple explicit scheme here, due to its ease of implementation despite there being a constraint on the stability in comparison to an implicit method. This method is also easily scaled up to 3D with little difficulty.

For the more complicated non-linear heat equation we have to account for the possibility that the medium is not continuously smooth between nodes, in terms of optical and thermal properties. The two easiest methods [55] of achieving this are: (1), lag the value behind by one step, i.e $c_p^{n+1} = c_p^n$. (2), average κ, ρ, and c_p using a half difference scheme where the thermal property used in the calculation is the thermal property half way between two nodes, i.e the average of the two nodes:

$$\kappa^{\pm} = \frac{\kappa_i + \kappa_{i\pm1}}{2} \tag{2.9}$$

$$\rho^{\pm} = \frac{\rho_i + \rho_{i\pm1}}{2} \tag{2.10}$$

$$c_p^{\pm} = \frac{c_{p,i} + c_{p,i\pm1}}{2} \tag{2.11}$$

Thus for the simple 1D case as in Eq. (2.8b), we average the thermal properties when computing the coefficients of the temperature nodes, and lag the thermal properties when adding the heat from the laser:

$$T^{N+1} = \Delta t(AT_{i-1}^N - 2BT_i^N + DT_{i+1}^N) + T_i^N + \frac{\Delta t\ \dot{q_L}}{\rho c_p} \tag{2.12}$$

Where (in the x direction):

$$\begin{aligned} A =& \frac{\kappa^-}{\rho^- c_p^- 2\Delta x^2} \\ B =& \frac{\kappa^+}{\rho^+ c_p^+ 2\Delta x^2} \\ D =& \frac{(A+B)}{2} \end{aligned} \tag{2.13}$$

Equation (2.12) is straightforward to generalise to higher dimensions. The 3D case gives:

$$U_{xx} = (AT^N_{i-1,j,k} - 2BT^N_{i,j,k} + DT^N_{i+1,j,k}) \tag{2.14}$$

$$U_{yy} = (AT^N_{i,j-1,k} - 2BT^N_{i,j,k} + DT^N_{i,j+1,k}) \tag{2.15}$$

$$U_{zz} = (AT^N_{i,j,k-1} - 2BT^N_{i,j,k} + DT^N_{i,j,k+1}) \tag{2.16}$$

$$T^{N+1}_{i,j,k} = \Delta t\ (U_{xx} + U_{yy} + U_{zz}) + T^N_{i,j,k} + \tfrac{\Delta t}{\rho c_p}\dot{q_L} \tag{2.17}$$

Where:
$T^{N+1}_{i,j,k}$ is the new temperature at node i, j, k $[K]$;
$T^N_{i,j,k}$ is the temperature at node i, j, k at the current time step $[K]$;
α is the thermal diffusivity $[m^2 s^{-1}]$;
κ is the thermal conductivity $[W/mK]$;
Δx *etc.* is the size of the grid element in the p^{th} direction $[m]$;
and A, B, D are the coefficients in their respective dimension (Eq. (2.13)).

Incorporating B.Cs on the top air exposed face:

$$U_{zz} = \tfrac{\alpha}{\Delta z^2}(\tfrac{2\Delta z}{\kappa}(-h(T^N_{i,j,k} - T^N_{\infty})) - 2T^N_{i,j,k} + 2T^N_{i,j,k+1}) \tag{2.18}$$

Equations (2.17) and (2.18) give the full numerical solution to the non-linear heat equation with a convection boundary term and laser heat source. This will allow us to calculate the heat diffusion in the porcine tissue due to laser heating.

As the laser used in the experimental work, operates in a pulsed mode, we account for this in our simulation. The laser pulse shape is a triangular pulse, with the peak power, P_{peak}, and pulse length, τ [56]. In the heat simulation we have an additional variable in the term $laserOn(t) \cdot \frac{\alpha\Delta t}{\kappa}\dot{q_L}$ in Eq. (2.17). This additional variable, $laserOn(t)$, is a boolean value and a function of time, which is defined as:

$$laserOn = \begin{cases} 1, & \text{Laser on} \\ 0, & \text{Laser off.} \end{cases}$$

In the instance where there is more than one pulse, the laser is turned on and off based upon the pulse frequency.

As we are using a simple explicit FDM, the time step is constrained in order to make the solution stable. For a cubic 3D FDM without prescribed flux BCs, yields the constraint: $\Delta t \leq \frac{1}{\delta\alpha}$ where $\delta = \frac{1}{\Delta x^2} + \frac{1}{\Delta y^2} + \frac{1}{\Delta z^2}$. However as there is also a convection boundary condition, the constraint on the timestep is more severe, due to the more mathematically complicated expressions [55].

However as we have a convection prescribed boundary condition, the constraint on the time is more severe. Along with this time constraint, the pulse length of the laser also has to be considered. If the time step of the heat simulation is too large it will not account for the heat deposited by the laser. Thus, the timestep has to be at least an order of magnitude smaller than the shortest laser pulse.

As the time step is small, and the grid resolution large, the resultant simulation is slow. Thus the code has been fully parallelised to improve performance. Both the MCRT and heat simulation are independently parallelised.

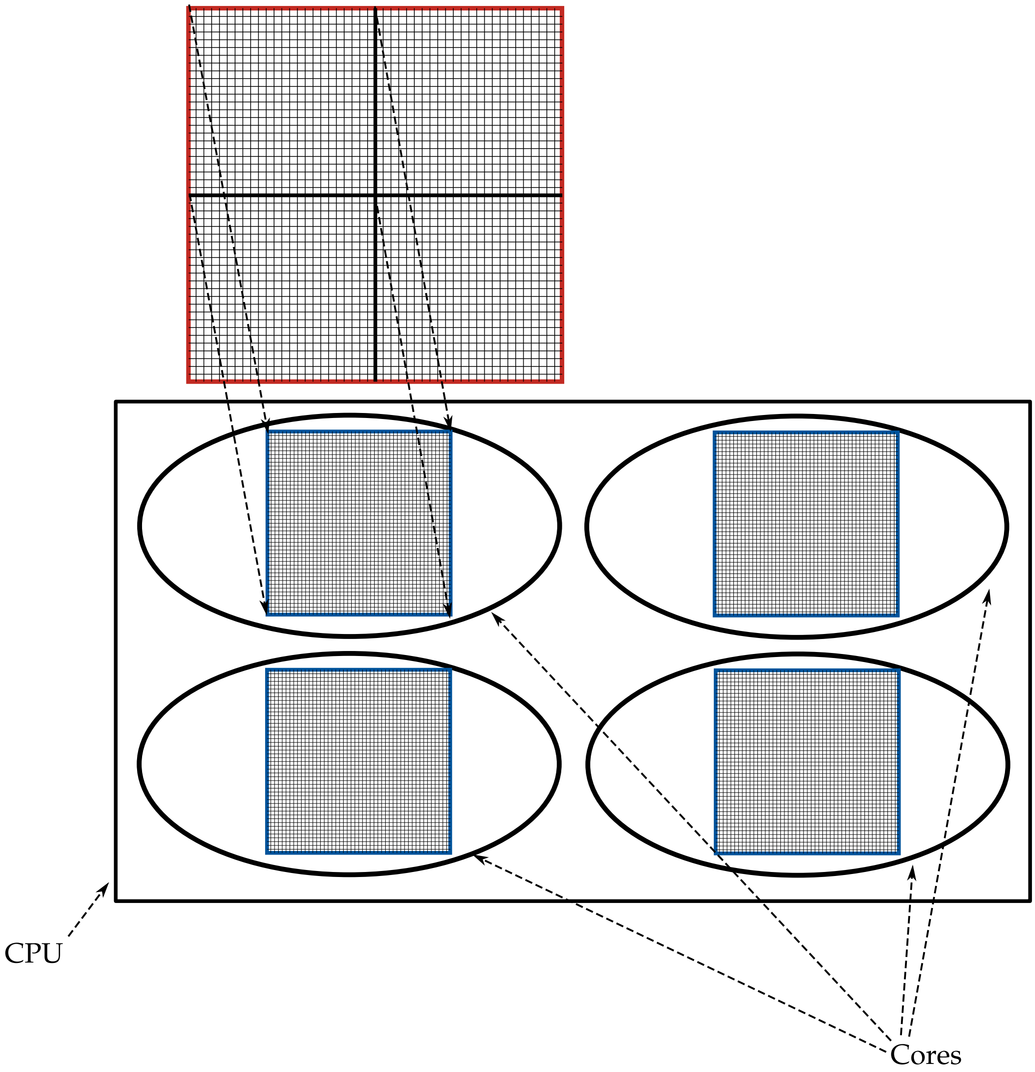

Figure 2.5: *Computational domain decomposition. Total computational domain (red outline) is evenly divided between cores in the CPU. This is done via layers of the domain in the z direction. Information is passed to/from cores via the 'halo swap' process (see Fig. 2.6).*

Parallelisation of the heat simulation is more involved than the 'embarrassingly parallel' class of problems that MCRT belongs to. This is due to the heat simulation being dependant on neighbouring nodes to update the temperature at the current node. Thus if we were to split up the medium on to separate cores, there would have to be communication between the cores, in order for the simulation to be completed successfully. Therefore we can not take the 'easy' route of running the simulation concurrently N times and collating the result at the end of all the simulations.

We parallelise the heat simulation using a technique called 'halo swapping'. This involves splitting up the computational domain (see Fig. 2.5), in this case the tissue medium, and doing the calculations on each domain on a separate core. The 'halo swapping' comes in when cores need to communicate with each other about updating their boundary temperature nodes (see Fig. 2.6).

Figure 2.7 shows the speed up gained from using the technique. The 'halo swapping' technique is efficient for situations where the computational domain can be split up with large 'chunks' being calculated on each core. However if the computational domain is small, and the number

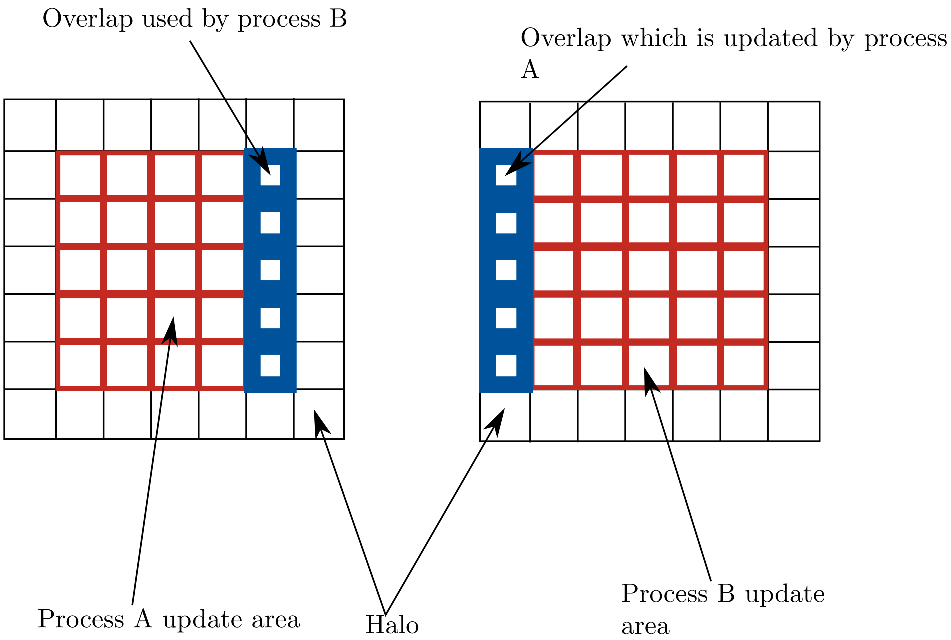
Overlap used by process B
Overlap which is updated by process A
Process A update area
Halo
Process B update area

Figure 2.6: *Halo swapping. Process A updates the area in red and blue on the left. It updates the blue area which is sent to process B as B's 'halo'. Process B cannot update it's own halo, but rather updates the halo for process A.*

Figure 2.7: *Figure show the speed up gained by parallelisation of the heat simulation using the 'halo' swapping technique, for various sizes of computational domain (voxels). Data taken from a Intel Xeon E3-1245 v5, 8 cores @ 3.5GHz machine.*

of cores large then bottlenecks occur due to too much communication between cores taking place. Thus to efficiently use 'halo swapping' careful thought has to be given to the size of the computational domain, and the number of cores running the simulation. Evidence of this bottlenecking can be seen in Fig. 2.7 for problems where the size of the grid, in voxels, is 40^3 and 24^3. These problems also show superlinear speed up, for certain number of cores. This is not unfeasible, due to a number of reason, in particular the underlying computer architecture [57].

After one time step of the heat simulation has been completed, the temperature grid is passed to the tissue damage portion of the simulation to calculate the tissue damage that may have accrued during the heat simulation time step.

2.2.3 Tissue Damage

2.2.3.1 Introduction

The final portion of the simulation is the tissue damage model. To be able to model damage to the tissue we first need to be able to describe the tissue damage process due to heating from a laser.

When the laser is turned on, the temperature starts to rise within the tissue due to the absorption of packets by the tissue. The temperature rise causes damage to the tissue when above a threshold temperature, T_d, approximately $43°C$ [58]. From the temperature, T_d, we define four main areas of tissue damage:

$$T = \begin{cases} \text{coagulation,} & T_d \leq T \leq 100\ °C \\ \text{water boils,} & T = 100\ °C \\ \text{carbonisation,} & 100\ °C \leq T \leq T_a \\ \text{ablation,} & T = T_a. \end{cases} \tag{2.19}$$

The area of tissue damage we term ‘coagulation’ is a multifaceted process. At 43°C - 50°C, bonds break within cell membranes, causing ruptures, and some cell death [58,59]. This process is usually termed *hyperthermia*. Around 50°C, enzyme activity decreases, cells become immobile, and various cell repair mechanisms are disabled, leading to increased cell death. When temperatures exceed 60°C, proteins become denatured. Thermal denaturation is a structural and functional change in a protein due to the heating it undergoes. This means they change from a highly organised structure with specific purposes, to disorganised structures with little to no function at all. [60]

The next stage in the tissue damage process is the vaporisation of water. As the temperature of the tissue starts to approach 100°C (at 1 atm), water starts to vaporise. If the vaporised water cannot escape the tissue it forms steam vacuoles, small pockets of steam. These vacuoles can easily been seen when viewing tissue samples after tissue has been treated with a high powered laser (see Fig. 2.8). In certain conditions these steam pockets can explode, with these ‘explosions’ being audible by the human ear [61].

The third stage of tissue damage is carbonisation or caramelisation of the tissue. This occurs when most of the water has boiled off, leaving the remaining tissue to heat up and reduce to its elemental carbon form. This carbonisation of tissue, when it occurs, is generally only a thin layer of 5-20 μm [58,62].

The final stage of tissue damage is the removal of the remaining tissue, i.e tissue ablation. There is no agreement in the literature how tissue undergoes ablation with a number of methods proposed [63,64]. The tissue ablation process is not a simple process, with various unknowns which depend on everything from tissue composition to laser power, wavelength, and pulse length. The literature however, does suggest that it takes place when the tissue temperature is between 177 and 500°C [65–67].

In order to model all these tissue damage processes we split our tissue damage model into two sections: ‘physical’ damage and coagulation damage. ‘Physical’ damage changes the tissue optical and thermal properties. Coagulation damage has no effect on the tissue’s bulk optical or thermal properties.

2.2.3.2 Modelling coagulation damage

With the description of the various process that tissue undergoes during ablation, we can now create a numerical model of these processes. First, in order to model the full extent of the

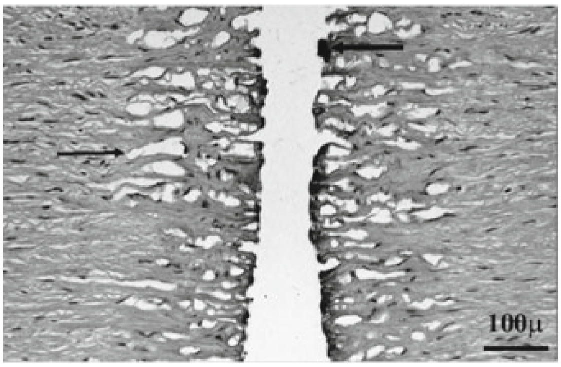

Figure 2.8: *Ablation of a dog aorta, as viewed under a microscope. Steam vacuoles are clearly visible either side of the ablation area. Carbonisation is also evident at the edges of the ablation fronts. Adapted from [58].*

damage done under 100°C, i.e in the coagulation regime, we use the Arrhenius damage model. The Arrhenius damage model was originally used as a kinetic model of reaction products in chemistry [68]. It has since been adapted by various authors for modelling tissue damage, and is the *de facto* standard [69, 70]. These authors and various others, adapted this model by fitting Eq. (2.20) to experimental data for burn damage. The two parameters fitted are A, the frequency factor, and ΔE, the activation energy.

$$\Omega(t) = \int_{t_i}^{t_f} A e^{(-\frac{\Delta E}{RT})} d\tau \tag{2.20}$$

Where:
Ω is the damage value;
A is ‘frequency factor’ $[s^{-1}]$;
ΔE is activation energy $[Jmol^{-1}]$;
R is the universal gas constant $[Jmol^{-1}K^{-1}]$;
T is the temperature $[K]$;
and t_i and t_f are the initial time and final time at t_{crit}.

It is reported that a value of Ω of 0.53, 1.0, and 10^4 relate to first, second, and third degree burns respectively [71]. We use the Arrhenius damage model in order to better understand the amount of damage caused by the laser in the non-ablated areas of tissue. We adopt of $A = 3.1 \times 10^{98}$, and $\Delta E = 6.27 \times 10^8$ for $T \leq 55$, and for $T > 55$ $A = 5 \times 10^{45}$, and $\Delta E = 2.96 \times 10^8$ [72].

2.2.3.3 Modelling physical tissue damage

As tissue mostly consists of water [40] when the temperature of the tissue approaches 100°C (at 1 atm), water in the tissue begins to boil off. This acts as a large heat sink for the absorbed laser energy, slowing down the rate of ablation. The energy required to boil the water is $Q_{vapor} = m_v \cdot L_v$, where m_v is the mass of a voxel, and L_v is the latent heat of vaporisation. The energy to boil off the water is provided via the laser and heat diffusing into the voxel:

$$Q_{vapor} = \underbrace{laserOn(t) \cdot \dot{q} \cdot \Delta t \cdot V_{i,j,k}}_{\text{laser heating}} + \underbrace{c \cdot M_{i,j,k} \cdot \Delta T}_{\text{heat diffusion}} \tag{2.21}$$

Where:

Q_{vapor} is the current energy in Joules that has been used to boil off the water in the voxel $[J]$;
$laserOn$ is a boolean variable that determine if the laser is on or off $[-]$;
$\dot{q}$ is the energy absorbed by the voxel due to the laser $[Wm^{-3}]$;
Δt is the timestep $[s]$;
$V_{i,j,k}$ is the volume of the voxel labelled i, j, k $[m^3]$;
c is the heat capacity of the voxel $[JK^{-1}]$;
$M_{i,j,k}$ is the mass of the the voxel labelled i, j, k $[kg]$;
and ΔT is the change in temperature the voxel would undergo, if the water was not boiling off.

As water boils off, the water content of each voxel changes. This affects the absorption coefficient, density, thermal conductivity, and heat capacity. Each of these vary with water content per voxel [73];

$$W = W_{init} - \left(W_{init} \cdot \left(\frac{Q_{current}}{Q_{vaporisation}}\right)\right) \tag{2.22}$$

$$\rho = \frac{1000}{W + 0.649 \cdot P} \tag{2.23}$$

$$c_p = 4.2 \cdot 10^3 \cdot W + 1.09 \cdot 10^3 \cdot P \tag{2.24}$$

$$\kappa = \rho \cdot (6.28 \cdot 10^{-4} \cdot W + 1.17 \cdot 10^{-4} \cdot P) \tag{2.25}$$

$$\mu_a = W \cdot \mu_{water} + \mu_{protein} \tag{2.26}$$

$$\tag{2.27}$$

Where:
W is the water content (i.e W = 0.7 equates to 70% water content);
W_{init} is the initial water content;
$Q_{current}$ is the total energy absorbed by the i^{th} voxel since the temperature reached 100°C $[J]$;
P is the protein content (i.e P = 1.0 - W);
κ is the Thermal conductivity $[Wm^{-1}K^{-1}]$;
c_p is the heat capacity $[Jkg^{-1}K^{-1}]$;
and μ_a is the total absorption coefficient, and μ_{water} and $\mu_{protein}$ are the absorption coefficients of water and protein respectively.

We define the T_a as occurring between 177 and 500°C [65–67]. At T_a the tissue is removed and the thermal, optical, and physical properties set to that of air.

The updated damaged tissue structure is then fed back to the MCRT model and the whole process repeats until the predefined time limit is reached. This whole process of photon propagation, heat diffusion and tissue damage is outlined in Fig. 2.1.

2.2.4 Validation

2.2.4.1 Heat transport validation

In order to thoroughly validate the numerical method we employ to solve the heat equation, we compare the numerical method against an easily solvable analytical case. We solve the heat equation on a cube, side L, in a surrounding medium of 0°C. The cube is initially at temperature 37°C and we calculate the temperature at time *t=0.1s*. Thus the boundary conditions are:

$$T(0,y,z,t) = T(x,0,z,t) = T(x,y,0,t) = 0°\mathrm{C} \tag{2.28}$$
$$T(L,y,z,t) = T(x,L,z,t) = T(x,y,L,t) = 0°\mathrm{C} \tag{2.29}$$

The thermal diffusivity (α), density (ρ), and heat capacity (c_p) are all set to 1. Assuming a separable solution in Cartesian coordinates yields:

$$\begin{aligned} T(x,y,z,t) =& (A_1 cos(\alpha x) + A_1 sin(\alpha x)) \cdot \\ & (B_1 cos(\beta y) + B_1 sin(\beta y)) \cdot \\ & (C_1 cos(\gamma z) + C_1 sin(\gamma z)) \cdot e^{-\alpha \mu^2 t} \end{aligned} \tag{2.30}$$

$$\mu^2 = \alpha^2 + \beta^2 + \gamma^2 \tag{2.31}$$

Applying the boundary conditions (Eqs. (2.28) and (2.29)) gives:

$$A_1 = B_1 = C_1 = 0 \text{ and } \alpha = \frac{\pi n}{L} \; \beta = \frac{\pi m}{L} \; \gamma = \frac{\pi p}{L} \tag{2.32}$$

$$\therefore T_{nmp}(x,y,z,t) = A_{nmp} \cdot sin\left(\frac{\pi n x}{L}\right) \cdot sin\left(\frac{\pi m y}{L}\right) \cdot sin\left(\frac{\pi p z}{L}\right) \tag{2.33}$$

This yields the following solution for the heat equation using the principle of superposition, and solving Eq. (2.34) with $f(x,y,z)$ as the initial temperature profile of the cube:

$$A_{nmp} = \frac{8}{L^3} \int_0^L \int_0^L \int_0^L f(x,y,z) \cdot sin(\frac{\pi n x}{L}) \cdot sin(\frac{\pi n y}{L}) \cdot sin(\frac{\pi n z}{L}) \; dx \cdot dy \cdot dz \tag{2.34}$$

$$T(x,y,z,t) = \sum_{n=1,3,..}^{\infty} \sum_{m=1,3,..}^{\infty} \sum_{p=1,3,..}^{\infty} \frac{2368}{\pi^3 nmp} \cdot sin(\frac{\pi n x}{L}) \cdot sin(\frac{\pi m y}{L}) \cdot sin(\frac{\pi p z}{L}) \cdot e^{(-\lambda^2 t)} \tag{2.35}$$

Where:
$\lambda^2 = \alpha \pi^2 (\frac{n^2}{L^2} + \frac{m^2}{L^2} + \frac{p^2}{L^2})$;
n, m, p are odd integers;
and L is the length of the cube.

At time, $t = 0.1$s, a slice through the middle of the cube, $L = 1\ cm$, yields Fig. 2.9, which shows that the numerical method matches the analytical solution closely.

2.2.4.2 MCRT & heat transport validation

As a first test of our code, both MCRT and heat simulation, we compare to a simple analytical model of ablation. The simple model of ablation is as: We define the ablation energy (E_a) as the minimum energy required to raise the temperature of the medium to 100 °C, and then boil off the water in a volume dV, mass M. Thus in one dimension we have Eq. (2.36), where the symbols have their usual meanings. If the energy for ablation is delivered in a time dt by a laser of power density ($W cm^{-2}$), P, this gives Eq. (2.37). Equation (2.37) can be rearranged in order to give an ablation front velocity, Eq. (2.38).

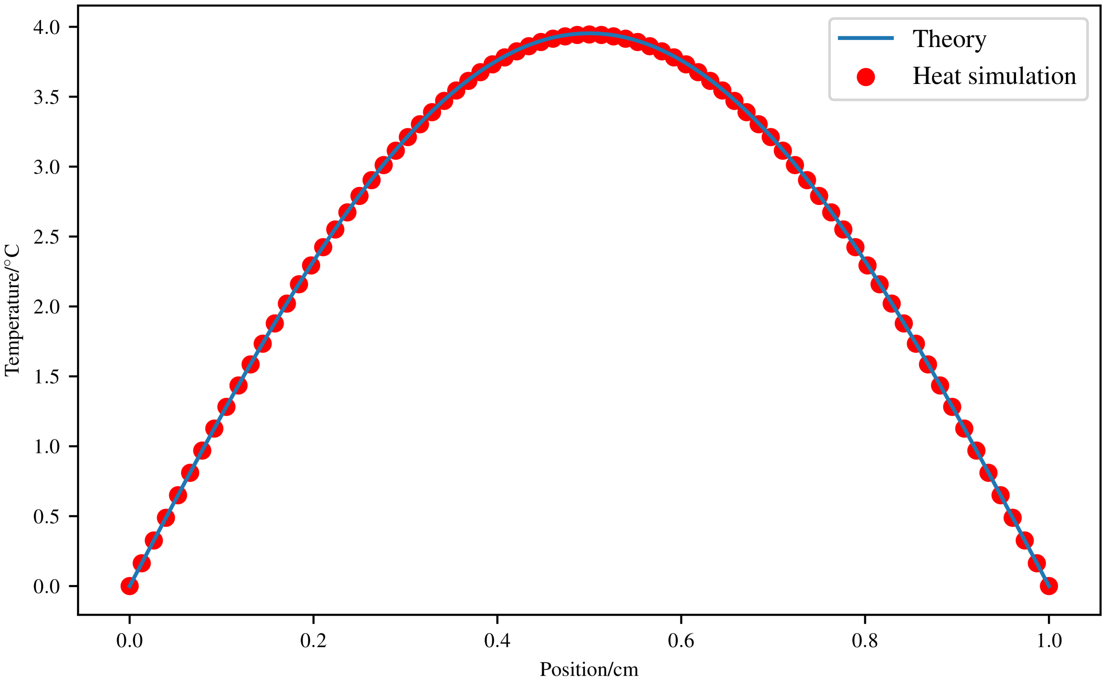

Figure 2.9: *Comparison between analytical solution and numerical method at t=0.1 s.*

$$E_a = c_p \rho dx \Delta T + L_v \rho dx \tag{2.36}$$

$$P \cdot dt = \rho dx (c_p \Delta T + L_v) \tag{2.37}$$

$$u = \frac{P}{\rho (c_p \Delta T + L_v)} \tag{2.38}$$

Assuming the ablation front moves with constant velocity during the ablation, and using $L_v = 2.53 \cdot 10^6 \ Jkg^{-1}$, $c_p = 4181 \ J \cdot kg^{-1} \cdot K^{-1}$ and the medium is a cube side 2 mm, with a starting temperature is 37 °C with a water content of 70% giving a density of 700 $kg \cdot m^{-3}$. For these parameters this gives an ablation velocity, $u \simeq 0.77 \ cm \cdot s^{-1}$, and a time to ablate through 2 mm of tissue of $\simeq 0.26 \ s$. As the code developed in this chapter simulates the diffusion of heat in a medium due to an incident laser, the expected time to ablate through the same medium should be slightly larger as heat diffuses away from the voxel while it is heated being heated. When the full heat + MCRT code is used to simulate this experiment, it gives a time, $t \simeq 0.33 \ s$.

2.3 *In silco* results

2.3.1 Introduction

In order to match the experimental results, we must first create as accurate model of the experimental setup *in silico*. However due to computational constraints, such as memory and time available, we must make some approximations to the experimental set-up. The porcine skin was a large thin slice of the top most layers of the skin. However as the area of interest is where the ablation occurs, we initially model the porcine skin as a cuboid, dimensions: 1.1 × 1.1 × 0.5 cm. The initial temperature of the porcine skin is assumed to be around 5°, as the tissue

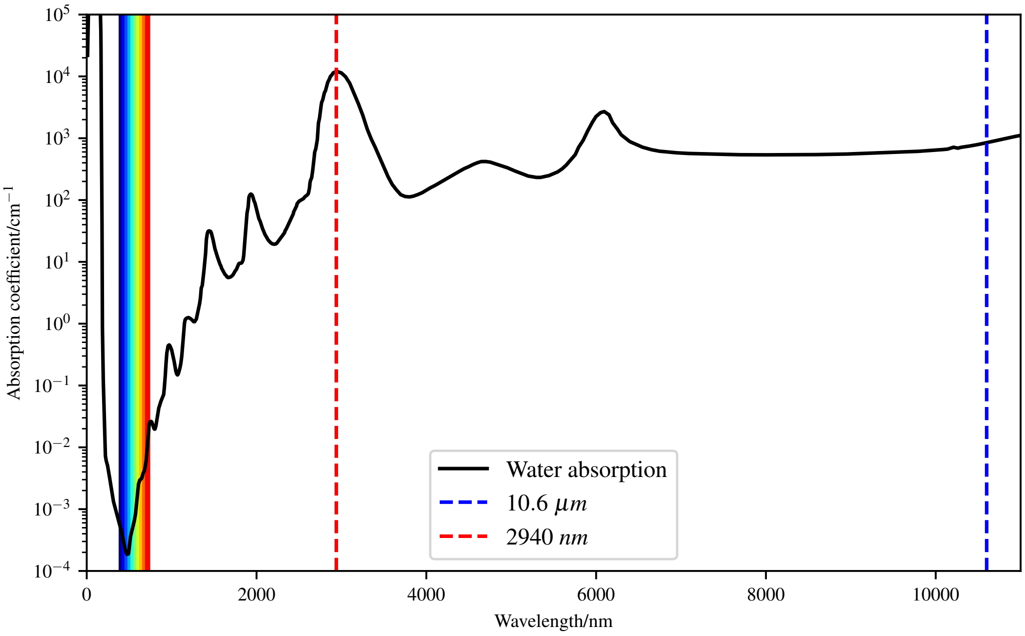

Figure 2.10: *Water absorption coefficient for wavelengths 0-12000nm [33]. Data shows that water is highly absorbing in the infra-red portion of the spectrum compared to the visible portion.*

was kept on ice or was kept cooled. As mentioned in the previous sections, there are several unknowns in the model: T_a, water content, temperature of air after ablation, and the exact thermal and optical properties of the porcine tissue. Therefore we run several models so that the full parameter space of these unknowns can be explored. Results from these *in silico* experiments are presented in this section along with a comparison of the model to the experimental work carried out in collaboration with the University of Dundee and the Photobiology department at Ninewells hospital.

2.3.1.1 Optical & thermal properties

The thermal and optical properties of porcine tissue are not known exactly for any given tissue sample. As such the thermal and optical properties used in this section are taken from various literature sources.

The laser used in the experimental work is an CO_2 laser operating at 10.6 μm. This means that the optical properties of the tissue are dominated by water absorption (see Fig. 2.10). The laser used in the experiment is the Pixel CO_2 [74]. The Pixel CO_2 laser has a wavelength 10.6 μm which corresponds to an absorption of coefficient in water of $\sim 850\ cm^{-1}$. As the absorption coefficient is large, we assume that scattering is negligible at these wavelengths. Table 2.1 summarises the thermal properties for tissue and air used in the simulations.

The laser was used in ‘Pixel beam’ mode. This means that the laser beam is split into an array of smaller beams. The laser used an array 9×9 of 81 pixel beams, each with a spot size of 250 μm. The Pixel CO_2 laser was upgraded during the period in which the experimental data was taken, we present both sets of data, pre-upgrade and post-upgrade. The upgrade consisted

	Thermal conductivity, κ	Density, ρ	Heat capacity, c
Tissue	$\rho \cdot (6.28 \cdot 10^{-4} \cdot W + 1.17 \cdot 10^{-4} \cdot P)$	$\frac{1000}{W+0.649 \cdot P}$	$4.2 \cdot 10^3 \cdot W + 1.09 \cdot 10^3 \cdot P$
Air	$ae^{-b(T-273.15)} + c$	$\frac{p_{atm}}{R_{spec}T}$	1006

Table 2.1: *Optical and thermal properties for porcine tissue and air.*

of an update to the laser power, from $\sim 30\ W$ to $\sim 70\ W$.

The laser delivered one single pulse of varying total energy delivered over the range 50 mJ to 400 mJ, in so called "super pulsed mode". The experiment consisted of ablating the porcine tissue, as a function of energy per 'pixel' beam. This was achieved by adjusting the pulse length of the laser, τ, so that the energy per pulse was varied over a range 50 mJ to 400 mJ. The energy range for the laser was kept the same pre and post-upgrade, with the pulse length differing.

2.3.1.2 Computational speed up:

As discussed in the Section 2.1, the volume of interest is the area around the ablation craters. The volume is 1.1 $cm \times 1.1\ cm \times 0.5\ cm$. However, in order for the simulation to have good resolution of the ablation craters, this volume would require a large number of voxels for the tissue model. This is unfeasible due to: the memory required to store the various counters, grids, and variables, and the time that would be required in order to carry out the computation. Thus the volume of interest is reduced to focus on just one of the ablation craters that is created by the laser. A volume of 0.06 $cm \times 0.06\ cm \times 0.18\ cm$ As a check to ensure that we are not omitting any phenomena by focusing on just one ablation crater, an initial simulation that simulates the full volume of interest was carried out to investigate the possibility of overlapping craters or other related phenomena. The simulation, as shown in Fig. 2.11, gives us validation that the shrinking of the volume of interest is a valid approximation to make, as there is no overlap between the separate ablation crater.

2.3.2 Results

2.3.2.1 Investigating ablation temperature, T_a

Various literature sources report the ablation temperature ranging from 177° to 500° [65–67]. Thus, we run several models over this range in order to establish a 'good' T_a which fits with the experimental results. Figures 2.12 and 2.13 show how T_a, and beam profile affect the crater depth as a function of pixel beam energy for the CO_2 laser. Simulation data suggests that, a 'good' T_a is around $T_a = 450\ °C$.

Increasing the ablation temperature, has the obvious effect of requiring more energy to be deposited by the laser before ablation takes place. This also allows more heat to diffuse away from the ablation crater increasing the thermal damage done to the surrounding tissue. Decreasing the ablation temperature has the converse affect, and allows the ablation crater to become deeper.

Over the full range of T_a, as the energy per pixel beam increases, there is a trend that at higher energies the crater depth begins to taper off. This is potentially due to a number of reasons. As the ablation craters grows the volume of tissue that is ablated is replaced with air, allowing more heat loss from the tissue to the environment. As well as heat loss to the environment, more heat is diffused away into the surrounding tissue as the crater grow, due to the availability of more tissue for the heat to diffuse into.

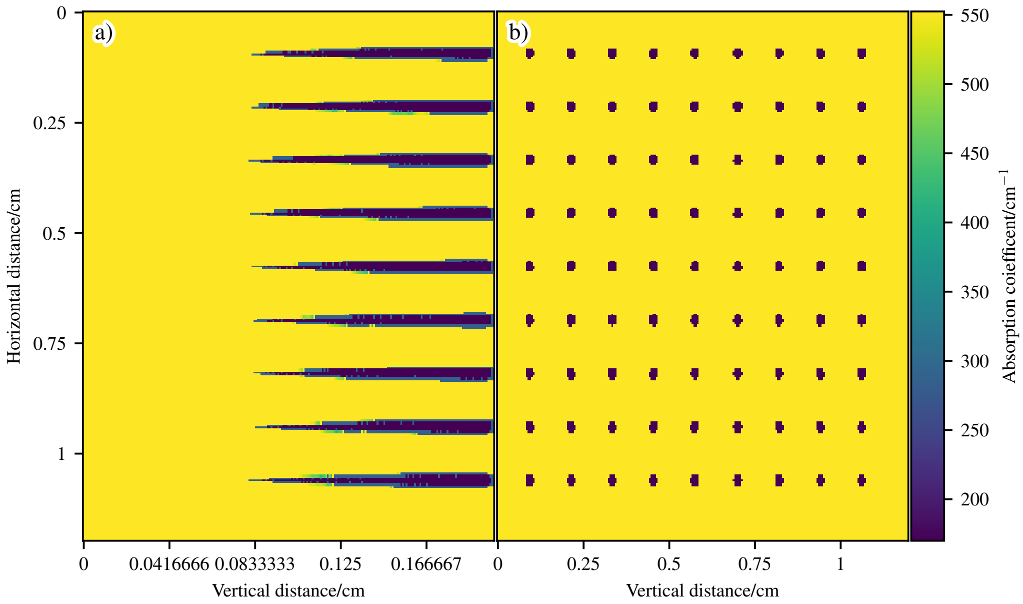

Figure 2.11: *Simulation of 81 pixel beams. Figure shows a a slice through the optical properties at the end of the simulation. Yellow is unchanged tissue, and purple is completely ablated tissue. Figure shows that the ablation craters do not overlap one another.*

2.3.2.2 Investigating beam type

As the manufacturer does not provide information on the beam profile of the pixel beams, we have to assume the shape of the beam profiles. We tried two different shapes: Gaussian, and circular. Figures 2.12 and 2.13 show the result of these *in-silico* experiments. The Gaussian beam ablates deeper holes than the circular beam type, which is to be expected due to the distribution of power in the Gaussian beam. The beam that best fits the data, is the circular beam. For the Gaussian beam to fit the data 'well' ablation would have to take place at temperatures above $500°C$ which does not fit with the literature. Without knowing the exact profile of the beam, we assume for the rest of the *in-silico* experiments that the beam profile is circular.

2.3.2.3 Investigating thermal damage

As stated in Section 2.2.3.2, we use the Arrhenius damage integral in order to estimate the thermal damage due to the laser. In order to calculate the tissue damage around the ablation craters, we first transform Eq. (2.20) in to a summation:

$$\Omega(t) = \int_{t_p}^{t_f} Ae^{(-\frac{\Delta E}{RT})} d\tau \tag{2.39}$$

$$\Omega(t) = \sum_{m=m_p}^{m_f} Ae^{(-\frac{\Delta E}{RT_{\xi}^{m}})} \Delta t \tag{2.40}$$

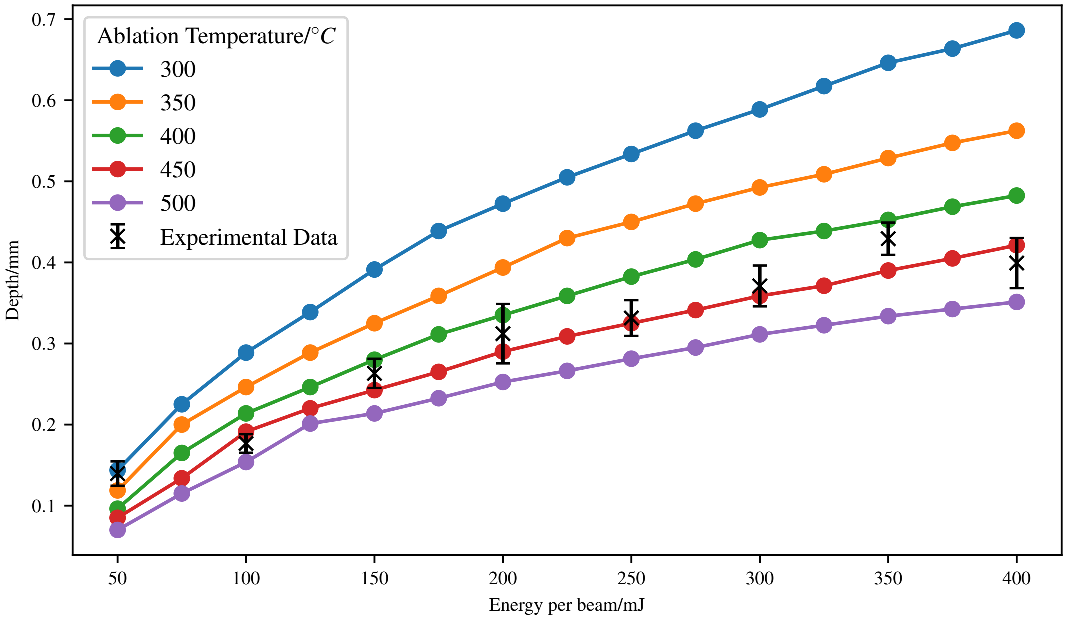

Figure 2.12: *Simulation of 70 W CO_2 ablative laser, with a circular beam profile. Crater depths as a function of pixel beam energy for various T_a's.*

Where:

ΔE, R, T, and A have the same meanings as before;
ξ is the i^{th}, j^{th}, k^{th} node;
and m_p is the p^{th} timestep when the ξ^{th} node is above the threshold temperature.

Using Eq. (2.40) we can thus estimate the damage to the tissue on a voxel by voxel basis. Figure 2.14 show how far the thermal damage extends around the ablation crater. For ease of visualisation we map 1-3 to their respective burns via the following scheme, with η as burn severity:

$$\eta = \begin{cases} 3, & \Omega \geq 10000 \\ 2, & 1 \leq \Omega < 10000 \\ 1, & 0.53 \leq \Omega < 1 \\ 0, & 0.0 \leq \Omega < 0.53. \end{cases} \tag{2.41}$$

As shown in Fig. 2.14, the thermal damage zone extends for a small distance around the ablation crater, due to the diffusion of heat into these areas. Figure 2.15 shows the maximum horizontal thermal damage distance as a function of T_a, and pixel beam energy. For values of T_a less than $\sim 425\ ^{\circ}C$, it appears that the maximum horizontal extent of the thermal damage tapers off. This is most likely due to the fact that for lower values of T_a, there is a a larger ablation crater, meaning that the energy form the laser is deposited deeper in the tissue in comparison to higher values of T_a. The higher values of of T_a allow greater diffusion of the heat, thus yielding larger zones of damage.

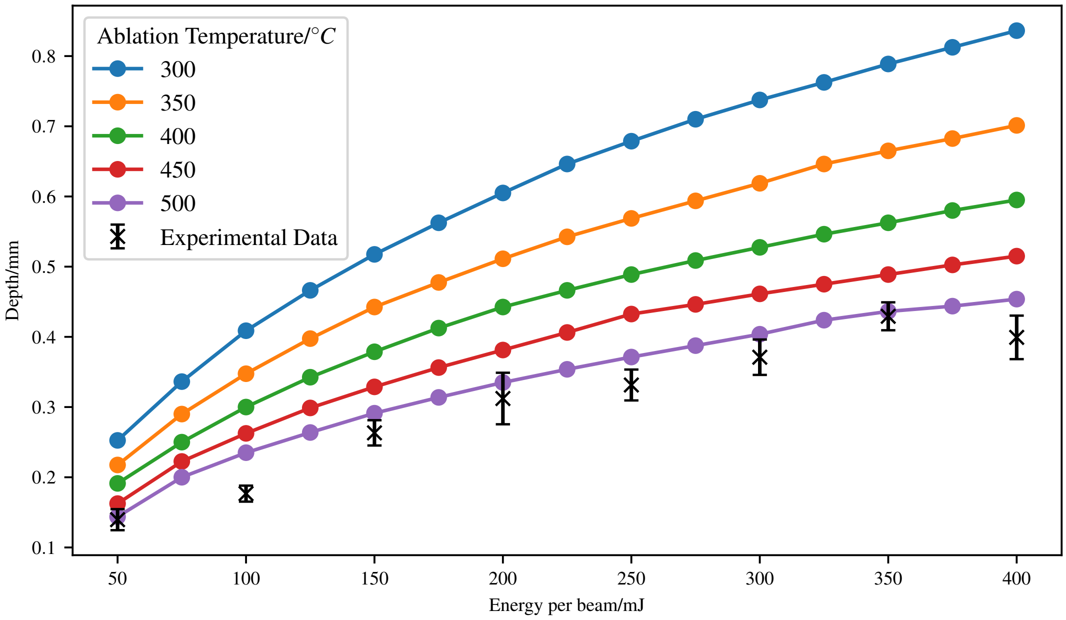

Figure 2.13: *Simulation of 70 W* CO_2 *ablative laser, with a Gaussian beam profile. Crater depths as a function of pixel beam energy for various* T_a*'s.*

We can also investigate the time it takes for different areas of the tissue to become thermally damaged. This can be easily achieved by saving the time each voxel passes one of the damage boundaries in Eq. (2.41). Figures 2.16 and 2.17 show the minimum time taken for 1^{st}, 2^{nd}, and 3^{rd} degree burns to occur as a function of depth. Figure 2.16 shows that there is little to no time (upon the order of 0.5 ms) between 1^{st} and 2^{nd}, and 3^{rd} degree burns. Figure 2.17 shows there is a slightly greater time difference between 1^{st} and 2^{nd}, and 3^{rd} degree burns, however this is almost as negligible as the 400 mJ case.

The reason that there is almost no time between 1^{st} and 2^{nd}, and 3^{rd} degree burns, is most likely due to the fact that there is very little time for heat to diffuse, whilst the laser is still illuminating the medium. The laser pulses are on the order of seconds, and tissue is not very thermally conductive. This leads to the results presented here.

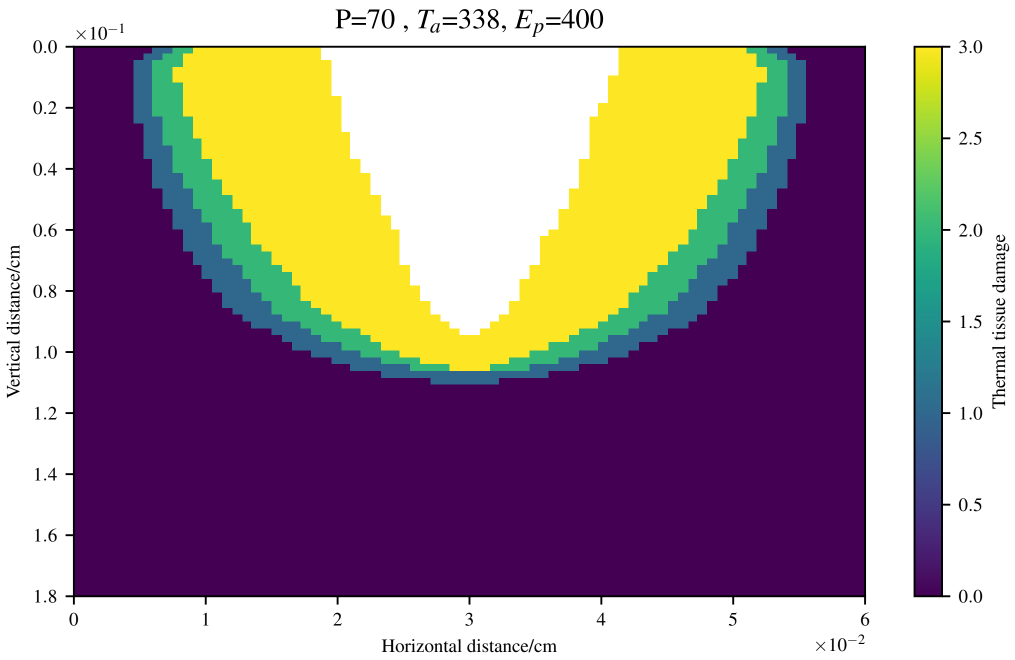

Figure 2.14: *Tissue thermal damage around the ablation crater (white). Thermal tissue damage values of 3 refer to 3^{rd} degree burns, 2 to 2^{nd}, and 1 to 1^{st} degree burns respectively. P is the power in Watts, T_a is the ablation temperature in Kelvin, and E_p is the energy per pixel beam in mJ.*

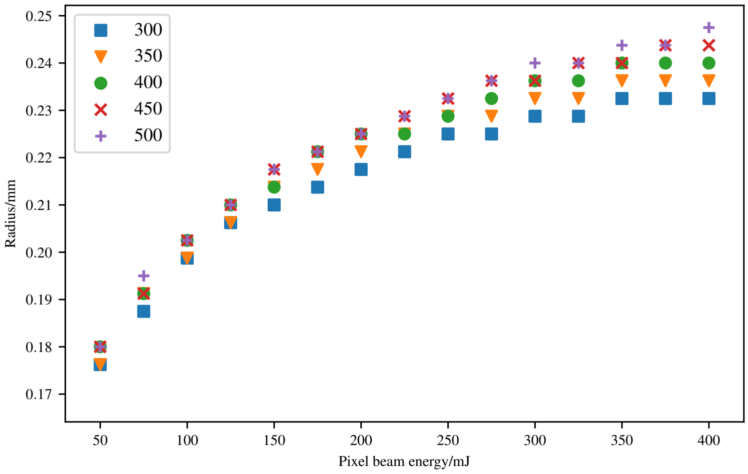

Figure 2.15: *Figure shows the maximum horizontal extent of thermal damage as a function of energy per pixel beam, for different T_a's.*

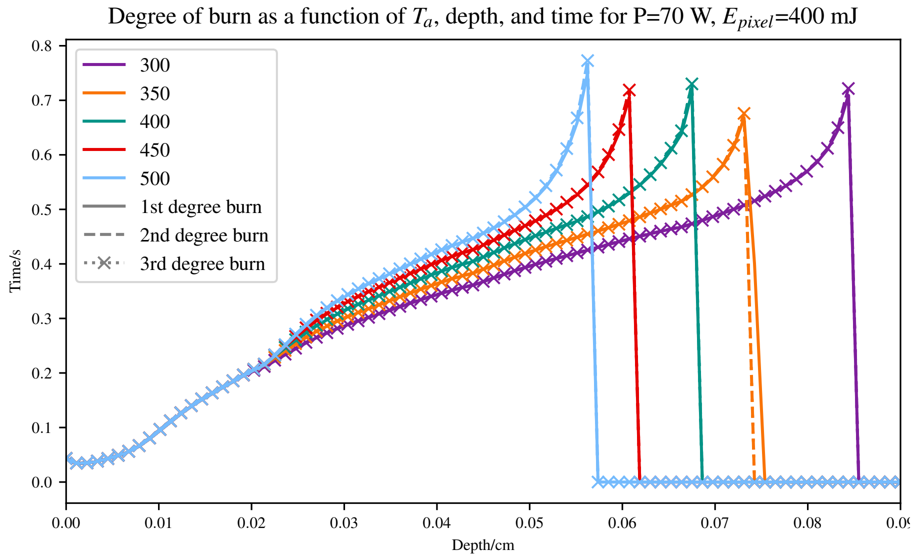

Figure 2.16: *Figure show the time taken for* 1^{st}, 2^{nd}*,and* 3^{rd} *to occur as a function of depth, for a range of* T_a*'s at 400 mJ.*

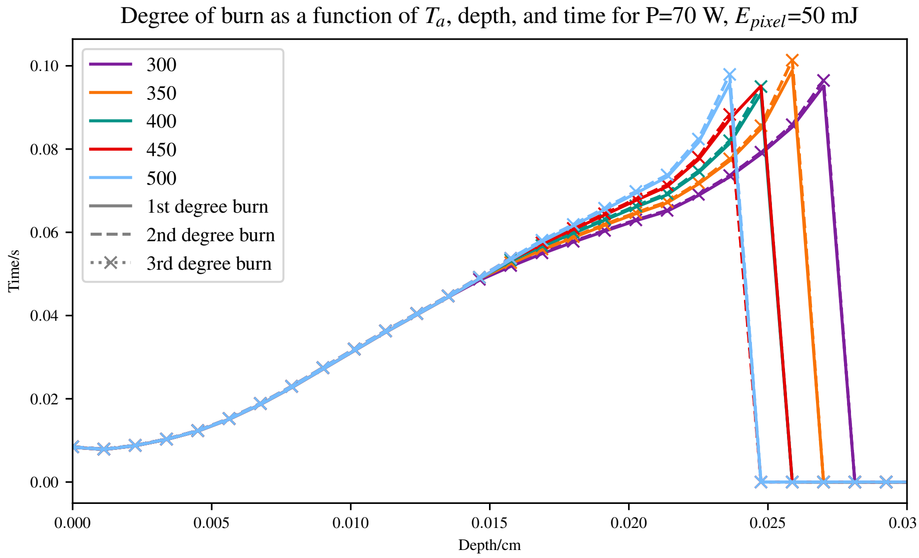

Figure 2.17: *Figure show the time taken for* 1^{st}, 2^{nd}*,and* 3^{rd} *to occur as a function of depth, for a range of* T_a*'s at 50 mJ.*

2.4 Conclusion

Using MCRT and a finite difference method, we have created a fully 3D model of photon and heat transport within tissue. This model can be used to simulate the heat deposited by laser, the ablation craters formed via high powered lasers and the resultant thermal damage surrounding the ablation crater.

Our model has been fully validated against both analytical solutions and experimental results. We found that to match with experimental results that a tissue ablation temperature T_a of around 420 K has to be adopted.

The simulations allow us to predict for a given laser power and pulse length, how much thermal damage is caused in the tissue, and how deep an ablation crater that will form. The computational model could be used in future to help develop treatment regimes for both aesthetic and medical procedures. For example, currently there is a lot of ‘down time’ after skin rejuvenation, in which the patient displays inflammation, erythema, edema, pain, and crusting [75–77]. Simulations of thermal damage due to fractional ablation could help design treatment regimes that minimise these effects, whilst still delivering skin rejuvenation. The model can also be applied to help optimise laser assisted drug delivery. Laser assisted drug delivery consists of using a laser to ‘drill’ holes into the skin in order to help topical medicines diffuse into the skin better, than just applying the medicines to skin with no holes. Our model can help predict the laser parameters needed to reach a certain hole depth, thus minimising thermal damage and pain to patients.

There are many avenues available with regards to future work on this model. The model presented here in this chapter was on a initially homogeneous skin model. In reality skin is compromised of several distinctive layers, with each layer containing varying amounts of different chromophores. Our model can easily incorporate an multi-layered skin model complete with various fractions of chromophores. The current model is a voxel based model, where all the voxels are the same size. This allows the model presented in this chapter to be easily set-up, with regards to parallelisation, optical/thermal properties and ease of programming. However voxel models, where all the voxels are the same size, are not computationally efficient. Particularly in order to achieve good resolution, many voxels are needed, which requires large amounts of RAM, due to a $\sim n^3$ scaling of voxels to memory in 3D. A more efficient way, would be to allow different sizes of voxels, depending on parts of the model which need high resolution, and parts that do not need high resolution. Such a voxel model is called an adaptive mesh refinement (AMR). There are downsides to AMR: complex implementation for parallelisation and set-up of optical/thermal properties, slower optical depth integration routines due to neighbour lookups.

Appendices

Appendix A

Heat equation derivation

To derive the heat equation we consider the conversation of energy in a volume R, with a flux out, $\phi(x, y, z, t)$, and unit outer normal $\hat{\mathbf{n}}$. We need just the normal component of $\phi : \phi \cdot \hat{\mathbf{n}}$.

The rate of change of heat inside the volume R is equal to the heat generated inside the volume R plus the heat flowing in/out of the boundary surface:

$$\text{Rate of change of heat energy} = \text{Rate of heat generation in R} + \text{Rate of heat energy flowing through boundary surface} \tag{A.1}$$

The total heat energy is:

$$e(x, y, z, t) = c(x, y, z) \cdot \rho(x, y, z) \cdot T(x, y, z, t) \tag{A.2}$$

and therefore the rate of change of heat energy is

$$\frac{d}{dt} \iiint\limits_{R} e \; dV = \frac{d}{dt} \iiint\limits_{R} c\rho T \; dV \tag{A.3}$$

We denote the heat generated inside the volume R as $Q(x, y, z, t)$:

$$\iiint\limits_{R} Q \; dV \tag{A.4}$$

and the rate of heat energy flowing through the boundary surface is:

$$-\iint\limits_{\partial R} \phi \cdot \hat{\mathbf{n}} \; dS^{[\ddagger]} \tag{A.5}$$

Substituting Eqs. (A.3) to (A.5) into Eq. (A.1), yields:

$$\frac{\partial}{\partial t} \iiint\limits_{R} c\rho T \; dV = -\iiint\limits_{R} \phi \cdot \hat{\mathbf{n}} \; dV + \iiint\limits_{R} Q \; dV \tag{A.6}$$

Using the divergence theorem, and simplifying gives:

[‡] This is negative as outward flow ϕ is positive, but the flow would result in a reduction of energy.

$$\frac{\partial}{\partial t}\iiint\limits_R c\rho T\ dV = -\iiint\limits_R \nabla\cdot\phi\ dV + \iiint\limits_R Q\ dV \tag{A.7}$$

$$\iiint\limits_R \left[c\rho\frac{\partial}{\partial t}T + \nabla\cdot\phi - Q\right] dV = 0 \tag{A.8}$$

Which holds for an arbitrary R, thus:

$$c\rho\frac{\partial}{\partial t}T = -\nabla\cdot\phi + Q \tag{A.9}$$

Using Fourier's law of heat conduction, which states that the local heat flux density, ϕ, is proportional to the negative local temperature gradient. The proportionality constant being equal to the thermal conductivity, κ:

$$\phi(x,y,z,t) = \kappa(x,y,z)\nabla T(x,y,z,t) \tag{A.10}$$

Substituting Eq. (A.10) into Eq. (A.9) yields the heat equation:

$$c\rho\frac{\partial}{\partial t}T = \nabla\cdot(\kappa\nabla T) + Q \tag{A.11}$$

Which can be simplified into the homogeneous medium heat equation with the following assumptions: Q=0 and $\kappa,\ \rho,\ and\ c$ are constant, and $\alpha = \frac{\kappa}{c\rho}$

$$\frac{\partial T}{\partial t} = \alpha\nabla^2 T \tag{A.12}$$

Bibliography

[1] Lee Badger. Lazzarini's lucky approximation of π. *Mathematics Magazine*, 67(2):83–91, 1994.

[2] Petr Beckmann. *A history of Pi.* St. Martin's Griffin, 2015.

[3] Georges-Louis Leclerc Buffon. *Histoire naturelle générale et particulière*, volume 18. de l'Imprimerie de F. Dufart, 1785.

[4] Peter Jäckel. *Monte Carlo methods in finance.* J. Wiley, 2002.

[5] David B Hertz. Risk analysis in capital investment. *Harvard Business Review*, 42(1):95–106, 1964.

[6] Jasper Vivian Wall and Charles R Jenkins. *Practical statistics for astronomers.* Cambridge University Press, 2012.

[7] James T. Kajiya. The rendering equation. *SIGGRAPH Comput. Graph.*, 20(4):143–150, August 1986.

[8] Robert L. Cook, Thomas Porter, and Loren Carpenter. Distributed ray tracing. *SIGGRAPH Comput. Graph.*, 18(3):137–145, January 1984.

[9] Nicholas Metropolis. The beginning of the Monte Carlo method. *Los Alamos Science*, 15:125–130, 1987.

[10] Roger Eckhardt. Stan Ulam, John von Neumann, and the Monte Carlo method. *Los Alamos Science*, 15:131–136, 1987.

[11] HL Anderson. Metropolis, Monte Carlo, and the MANIAC. *Los Alamos Science*, 14:96–108, 1986.

[12] Stanislaw Ulam, RD Richtmyer, and J Von Neumann. Statistical methods in neutron diffusion. *LAMS-551, Los Alamos National Laboratory*, pages 1–22, 1947.

[13] Kenneth Wood and RJ Reynolds. A model for the scattered light contribution and polarization of the diffuse hα galactic background. *The Astrophysical Journal*, 525(2):799, 1999.

[14] DWO Rogers, BA Faddegon, GX Ding, C-M Ma, J We, and TR Mackie. Beam: a monte carlo code to simulate radiotherapy treatment units. *Medical physics*, 22(5):503–524, 1995.

[15] BC Wilson and G Adam. A monte carlo model for the absorption and flux distributions of light in tissue. *Medical Physics*, 10(6):824–830, 1983.

[16] Lihong V Wang and Hsin-i Wu. *Biomedical optics: principles and imaging*. John Wiley & Sons, 2012.

[17] Subrahmanyan Chandrasekhar. *Radiative transfer*. Courier Corporation, 2013.

[18] Vesna Džimbeg-Malčić Željka Barbarić-Mikočević and Katarina Itrić. Kubelka-munk theory in describing optical properties of paper (i). *Technical Gazette*, 18(1):117–124, 2011.

[19] Marek Jasiński. Modelling of light and human skin interaction using kubelka-munk theory. *Scientific Research of the Institute of Mathematics and Computer Science*, 10(1):71–81, 2011.

[20] Wai-Fung Cheong, Scott A Prahl, and Ashley J Welch. A review of the optical properties of biological tissues. *IEEE journal of quantum electronics*, 26(12):2166–2185, 1990.

[21] Macaveiu Gabriela. Mathematical methods in biomedical optics. *ISRN Biomedical Engineering*, 2013, 2013.

[22] Reindert Graaff, Jan G Aarnoudse, Frits FM de Mul, and Henk W Jentink. Similarity relations for anisotropic scattering in absorbing media. *Optical engineering*, 32(2):244–253, 1993.

[23] Gilwon Yoon, Scott A Prahl, and Ashley J Welch. Accuracies of the diffusion approximation and its similarity relations for laser irradiated biological media. *Applied Optics*, 28(12):2250–2255, 1989.

[24] Thomas P Robitaille. On the modified random walk algorithm for monte-carlo radiation transfer. *Astronomy & Astrophysics*, 520:A70, 2010.

[25] M Min, CP Dullemond, C Dominik, Alex de Koter, and JW Hovenier. Radiative transfer in very optically thick circumstellar disks. *Astronomy & Astrophysics*, 497(1):155–166, 2009.

[26] Steven L Jacques. Origins of tissue optical properties in the uva, visible, and nir regions. *OSA TOPS on advances in optical imaging and photon migration*, 2:364–369, 1996.

[27] Steven L Jacques. Optical properties of biological tissues: a review. *Physics in Medicine & Biology*, 58(11):R37, 2013.

[28] Tom Lister, Philip A Wright, and Paul H Chappell. Optical properties of human skin. *Journal of biomedical optics*, 17(9):090901, 2012.

[29] Louis G Henyey and Jesse L Greenstein. Diffuse radiation in the galaxy. *The Astrophysical Journal*, 93:70–83, 1941.

[30] Steven L Jacques, CA Alter, and Scott A Prahl. Angular dependence of hene laser light scattering by human dermis. *Lasers Life Sci*, 1(4):309–333, 1987.

[31] James M Dixon, Masahiko Taniguchi, and Jonathan S Lindsey. Photochemcad 2: A refined program with accompanying spectral databases for photochemical calculations. *Photochemistry and photobiology*, 81(1):212–213, 2005.

[32] Scott Prahl. Photochemcad spectra. `https://omlc.org/spectra/PhotochemCAD/index.html`, 2017. [Online; Last accessed 4-February-2019].

[33] D.J. Segelstein. *The complex refractive index of water*. PhD thesis, University of Missouri–Kansas City, 1981.

[34] Robin M Pope and Edward S Fry. Absorption spectrum (380–700 nm) of pure water. ii. integrating cavity measurements. *Applied optics*, 36(33):8710–8723, 1997.

[35] Robert LP van Veen, HJCM Sterenborg, A Pifferi, A Torricelli, and R Cubeddu. Determination of vis-nir absorption coefficients of mammalian fat, with time-and spatially resolved diffuse reflectance and transmission spectroscopy. In *Biomedical Topical Meeting*, page SF4. Optical Society of America, 2004.

[36] Iyad Salam Saidi et al. *Transcutaneous optical measurement of hyperbilirubinemia in neonates*. PhD thesis, Rice University, 1992.

[37] Jose A Iglesias-Guitian, Carlos Aliaga, Adrian Jarabo, and Diego Gutierrez. A biophysically-based model of the optical properties of skin aging. In *Computer Graphics Forum*, volume 34, pages 45–55. Wiley Online Library, 2015.

[38] Alexey N Bashkatov, Elina A Genina, and Valery V Tuchin. Optical properties of skin, subcutaneous, and muscle tissues: a review. *Journal of Innovative Optical Health Sciences*, 4(01):9–38, 2011.

[39] Tadeusz Sarna and Harold A Swartz. The physical properties of melanins. *The pigmentary system: physiology and pathophysiology*, pages 311–341, 2006.

[40] I.V. Meglinski and S.J. Matcher. Quantitative assessment of skin layers absorption and skin reflectance spectra simulation in the visible and near-infrared spectral regions. *Physiological Measurement*, 23(4):741, 2002.

[41] Matthew D Keller, Robert H Wilson, Mary-Ann Mycek, and Anita Mahadevan-Jansen. Monte carlo model of spatially offset raman spectroscopy for breast tumor margin analysis. *Applied spectroscopy*, 64(6):607–614, 2010.

[42] Jon E Bjorkman and Kenneth Wood. Radiative equilibrium and temperature correction in monte carlo radiation transfer. *The Astrophysical Journal*, 554(1):615, 2001.

[43] Thomas P Robitaille. Hyperion: an open-source parallelized three-dimensional dust continuum radiative transfer code. *Astronomy & Astrophysics*, 536:A79, 2011.

[44] D. Manstein, G.S. Herron, R.K. Sink, H. Tanner, and R.R. Anderson. Fractional photothermolysis: a new concept for cutaneous remodeling using microscopic patterns of thermal injury. *Lasers in Surgery and Medicine: The Official Journal of the American Society for Laser Medicine and Surgery*, 34(5):426–438, 2004.

[45] S. Amini-Nik, D. Kraemer, M.L. Cowan, K. Gunaratne, P. Nadesan, B.A. Alman, and R.J. Dwayne Miller. Ultrafast mid-ir laser scalpel: protein signals of the fundamental limits to minimally invasive surgery. *PLoS One*, 5(9):e13053, 2010.

[46] O.T. Tan, K. Sherwood, and B.A. Gilchrest. Treatment of children with port-wine stains using the flashlamp-pulsed tunable dye laser. *New England Journal of Medicine*, 320(7):416–421, 1989.

[47] M. Kuperman-Beade, V.J. Levine, and R. Ashinoff. Laser removal of tattoos. *American Journal of Clinical Dermatology*, 2(1):21–25, 2001.

[48] S.H. Liew. Laser hair removal. *American Journal of Clinical Dermatology*, 3(2):107–115, 2002.

[49] C.A. Hardaway and E.V. Ross. Nonablative laser skin remodeling. *Dermatologic Clinics*, 20(1):97–111, 2002.

[50] S.M. Shapshay, M.S. Strong, G.W. Anastasi, and C.W. Vaughan. Removal of rhinophyma with the carbon dioxide laser: a preliminary report. *Archives of Otolaryngology*, 106(5):257–259, 1980.

[51] R. Valcavi, F. Riganti, A. Bertani, D. Formisano, and C.M. Pacella. Percutaneous laser ablation of cold benign thyroid nodules: a 3-year follow-up study in 122 patients. *Thyroid*, 20(11):1253–1261, 2010.

[52] M. Hædersdal, F.H. Sakamoto, W.A. Farinelli, A.G. Doukas, J. Tam, and R.R. Anderson. Fractional CO2 laser-assisted drug delivery. *Lasers in Surgery and Medicine: The Official Journal of the American Society for Laser Medicine and Surgery*, 42(2):113–122, 2010.

[53] M.R. Alexiades-Armenakas, J.S. Dover, and K.A. Arndt. The spectrum of laser skin resurfacing: nonablative, fractional, and ablative laser resurfacing. *Journal of the American Academy of Dermatology*, 58(5):719–737, 2008.

[54] D.V Widder. *The Heat Equation*, volume 67. Academic Press, 1976.

[55] N. Ozisik. *Finite Difference Methods in Heat Transfer.* CRC press, 1994.

[56] Alma Lasers GmbH. *PixelCO2 Operator's Manual.* Alma Lasers GmbH.

[57] Sasko Ristov, Radu Prodan, Marjan Gusev, and Karolj Skala. Superlinear speedup in hpc systems: Why and when? In *Computer Science and Information Systems (FedCSIS), 2016 Federated Conference on*, pages 889–898. IEEE, 2016.

[58] A.J Welch, M.J.C Van Gemert, et al. *Optical-thermal Response of Laser-irradiated Tissue*, volume 2. Springer, 2011.

[59] N.T. Wright. Quantitative models of thermal damage to cells and tissues. In *Heat Transfer and Fluid Flow in Biological Processes*, pages 59–76. Elsevier, 2015.

[60] M.H. Niemz. *Laser-tissue interactions: fundamentals and applications.* Springer Science & Business Media, 2013.

[61] F. Petrella, S. Cavaliere, and L. Spaggiari. Popcorn effect. *Journal of Bronchology & Interventional Pulmonology*, 20(2):193–194, 2013.

[62] R.M. Verdaasdonk, C. Borst, and M.J.C. Van Gemert. Explosive onset of continuous wave laser tissue ablation. *Physics in Medicine & Biology*, 35(8):1129, 1990.

[63] A. Vogel and V. Venugopalan. Mechanisms of pulsed laser ablation of biological tissues. *Chemical Reviews*, 103(2):577–644, 2003.

[64] A.L. McKenzie. Physics of thermal processes in laser-tissue interaction. *Physics in Medicine & Biology*, 35(9):1175, 1990.

[65] M. Gerstmann, Y. Linenberg, A. Katzir, and S. Akselrod. Char formation in tissue irradiated with a CO 2 laser: model and simulations. *Optical Engineering*, 33(7):2343–2352, 1994.

[66] A.L. McKenzie. A three-zone model of soft-tissue damage by a CO2 laser. *Physics in Medicine & Biology*, 31(9):967, 1986.

[67] A. Sagi, A. Avidor-Zehavi, A. Shitzer, M. Gerstmann, S. Akselrod, and A. Katzir. Heating of biological tissue by laser irradiation: temperature distribution during laser ablation. *Opt. Eng*, 31(7):1425–1431, 1992.

[68] J.A. Pearce. Relationship between arrhenius models of thermal damage and the cem 43 thermal dose. In *Energy-based Treatment of Tissue and Assessment V*, volume 7181, page 718104. International Society for Optics and Photonics, 2009.

[69] F.C. Jr Hendriques. Studies of thermal injury; the predictability and the significance of thermally induced rate processes leading to irreversible epidermal injury. *Arch. Pathol.(Chic)*, 43:489–502, 1947.

[70] S.C. Jiang, N. Ma, H.J. Li, and X.X. Zhang. Effects of thermal properties and geometrical dimensions on skin burn injuries. *Burns*, 28(8):713–717, 2002.

[71] K.R. Diller and L.J. Hayes. A finite element model of burn injury in blood-perfused skin. *Journal of Biomechanical Engineering*, 105(3):300–307, 1983.

[72] H. Ye and S. De. Thermal injury of skin and subcutaneous tissues: A review of experimental approaches and numerical models. *Burns*, 43(5):909–932, 2017.

[73] B.R. Loiola, H.R.B. Orlande, and G.S. Dulikravich. Thermal damage during ablation of biological tissues. *Numerical Heat Transfer, Part A: Applications*, pages 1–17, 2018.

[74] Alma Lasers. Pixel CO2, 2018.

[75] M. Lapidoth, S. Halachmi, S. Cohen, and D.B. Amitai. Fractional co2 laser in the treatment of facial scars in children. *Lasers in Medical Science*, 29(2):855–857, 2014.

[76] M.A. Trelles, M. Shohat, and F. Urdiales. Safe and effective one-session fractional skin resurfacing using a carbon dioxide laser device in super-pulse mode: a clinical and histologic study. *Aesthetic Plastic Surgery*, 35(1):31–42, 2011.

[77] E. Kohl, J. Meierhöfer, M. Koller, F. Zeman, L. Groesser, S. Karrer, U. Hohenleutner, M. Landthaler, and S. Hohenleutner. Fractional carbon dioxide laser resurfacing of rhytides and photoaged skin–a prospective clinical study on patient expectation and satisfaction. *Lasers in Surgery and Medicine*, 47(2):111–119, 2015.